Solar Irradiance Nowcasting Case Studies near Sacramento

JARED A. LEE, SUE ELLEN HAUPT, AND PEDRO A. JIMÉNEZ

Research Applications Laboratory, National Center for Atmospheric Research,[a] *Boulder, Colorado*

MATTHEW A. ROGERS AND STEVEN D. MILLER

Cooperative Institute for Research in the Atmosphere, Colorado State University, Fort Collins, Colorado

TYLER C. MCCANDLESS

Research Applications Laboratory, National Center for Atmospheric Research, Boulder, Colorado

(Manuscript received 12 May 2016, in final form 27 September 2016)

ABSTRACT

The Sun4Cast solar power forecasting system, designed to predict solar irradiance and power generation at solar farms, is composed of several component models operating on both the nowcasting (0–6 h) and day-ahead forecast horizons. The different nowcasting models include a statistical forecasting model (StatCast), two satellite-based forecasting models [the Cooperative Institute for Research in the Atmosphere Nowcast (CIRACast) and the Multisensor Advection-Diffusion Nowcast (MADCast)], and a numerical weather prediction model (WRF-Solar). It is important to better understand and assess the strengths and weaknesses of these short-range models to facilitate further improvements. To that end, each of these models, including four WRF-Solar configurations, was evaluated for four case days in April 2014. For each model, the 15-min average predicted global horizontal irradiance (GHI) was compared with GHI observations from a network of seven pyranometers operated by the Sacramento Municipal Utility District (SMUD) in California. Each case day represents a canonical sky-cover regime for the SMUD region and thus represents different modeling challenges. The analysis found that each of the nowcasting models perform better or worse for particular lead times and weather situations. StatCast performs best in clear skies and for 0–1-h forecasts; CIRACast and MADCast perform reasonably well when cloud fields are not rapidly growing or dissipating; and WRF-Solar, when configured with a high-spatial-resolution aerosol climatology and a shallow cumulus parameterization, generally performs well in all situations. Further research is needed to develop an optimal dynamic blending technique that provides a single best forecast to energy utility operators.

1. Introduction

Installed solar energy capacity is steadily increasing both around the nation and around the world. As a weather-dependent, variable resource, energy utility and independent system operators (ISOs) require accurate forecasts of the solar power availability to continually balance supply and demand on the electrical grid. Accurate forecasts allow grid operators to optimize unit commitment and minimize the need for running baseline or spinning-reserve fossil fuel plants when unnecessary, which ultimately saves ratepayers money (Marquis et al. 2011; Mahoney et al. 2012) and benefits the environment by reducing carbon dioxide (CO_2) emissions as well as those of other pollutants. Grid operators need these forecasts on time horizons from minutes and hours ahead to several days ahead (Tuohy et al. 2015).

On clear days, the global horizontal irradiance (GHI), and hence the power generated by a given farm, can be calculated with relative ease. When clouds are present, however, GHI and power predictions become significantly more difficult. Important parameters include cloud-top height and geometric thickness, the solar geometry, and the cloud optical properties that determine transmittance and downwelling solar irradiance reaching the surface. Aerosol and water vapor concentrations also attenuate irradiance and must be properly accounted

---

[a] The National Center for Atmospheric Research is sponsored by the National Science Foundation.

Corresponding author e-mail: Jared A. Lee, jaredlee@ucar.edu

DOI: 10.1175/JAMC-D-16-0183.1

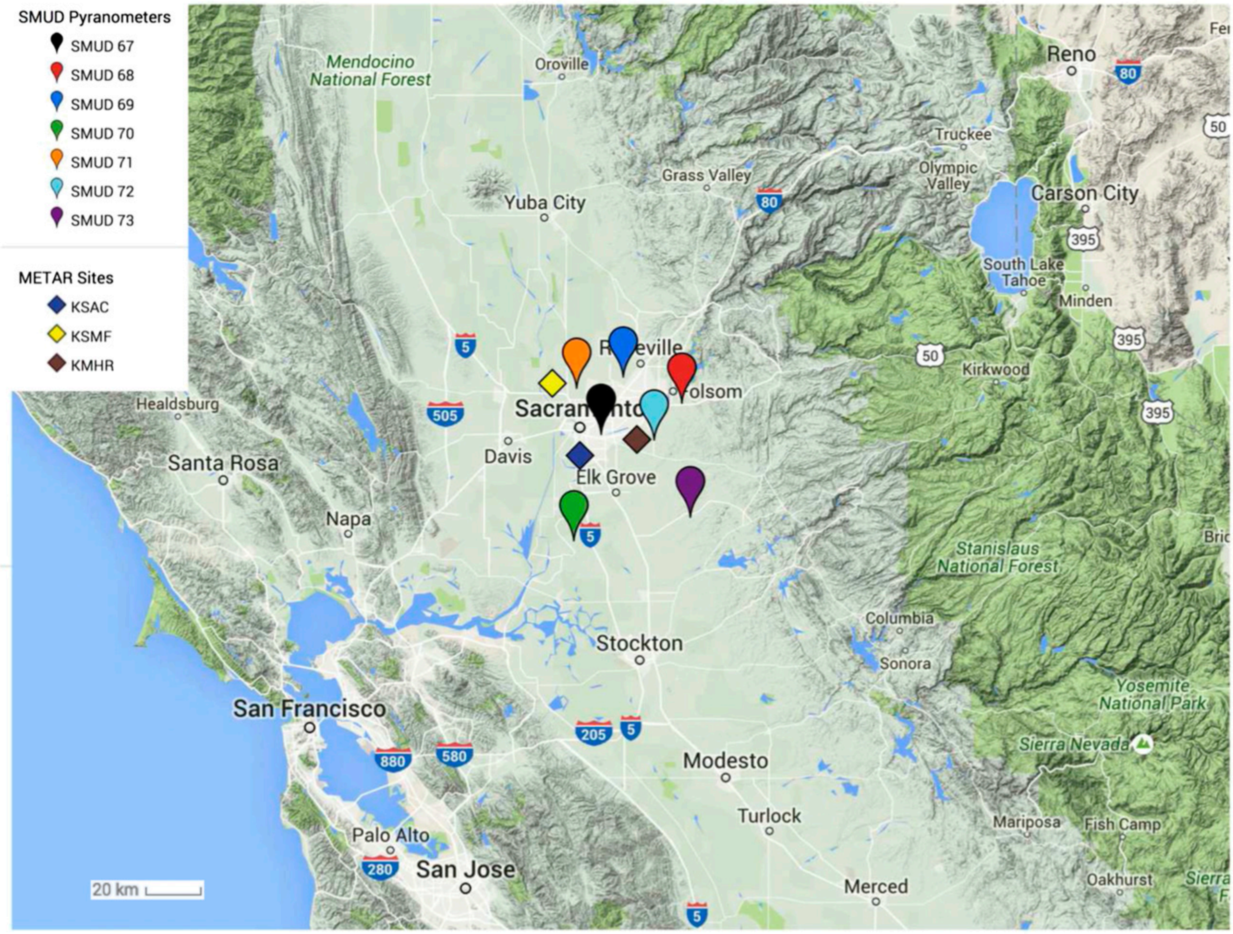

FIG. 1. Map of the locations of the SMUD pyranometers (colored "pins") and nearby METAR sites (colored diamonds).

for, especially because many types of aerosols function as cloud condensation nuclei or ice condensation nuclei; this is the aerosol indirect effect. Changes in a cloud field that shadows a solar panel array can cause significant ramps (rapid changes) in GHI, and therefore energy generated, in a matter of seconds to minutes. Reducing forecast errors in the timing and magnitude of these ramps is a primary goal of solar power forecasting. The regionally divided nature of the current U.S. electric grid and relatively small load balancing areas make ramp events even more crucial to predict accurately (e.g., MacDonald and Clack et al. 2016).

There are various techniques available to make nowcasts (short-range intraday forecasts on time scales of 0–6 h) of GHI. The first, and simplest, technique is a "smart persistence" forecast. Smart persistence forecasts begin with the most recent observations of GHI (or clearness index, which is the ratio of ground-level GHI to top-of-atmosphere GHI) and integrate them forward in time, accounting for changing solar zenith angle and the associated transmission adjustment. Particularly for forecast horizons of 30 min or less, GHI persistence forecasts are difficult to beat statistically (e.g., Perez et al. 2010, 2013; McCandless et al. 2016a).

A second technique is applying statistical machine learning algorithms to a large training dataset and the few most recent GHI observations. When properly trained and tuned, these methods can outperform persistence by leveraging historical observations, though the value of these predictions begins to wane after about 2–3 h (e.g., McCandless et al. 2015, 2016a,b). Diagne et al. (2013) and Inman et al. (2013) both provide

TABLE 1. Weights and threshold values for adjacent pixel group assignment in CIRACast.

Parameter	Threshold value	Effective weight
Same cloud type	—	0.35
Similar cloud type	—	0.25
Change in cloud-top height	2–3 km	0.30
Change in effective radius	5–10 μm	0.05
Change in cloud optical depth	5–10	0.05

TABLE 2. The 550-nm AOD values at 1800 UTC on each case day from the MERRAero dataset at the grid point nearest to Sacramento (38.5°N, 121.25°W).

Case	AOD
1 (17 Apr 2014)	0.115
2 (13 Apr 2014)	0.104
3 (22 Apr 2014)	0.072
4 (25 Apr 2014)	0.218

helpful overviews of recent developments in a multitude of solar energy forecasting techniques, not just with machine learning techniques, but also the other general techniques discussed below.

A third technique can be broadly defined as cloud tracking and cloud advection. Total-sky imagers (TSIs) and other ground-based cameras are used to identify and track clouds over a local area, though their forecast horizon is generally limited to a few minutes (Chow et al. 2011; Huang et al. 2013; Peng et al. 2015; Urquhart et al. 2015). Satellite imagery can also be used to identify cloud features and advect them based on either recent cloud motion or the wind field of a numerical weather prediction (NWP) model (Miller et al. 2011; Aulign√© 2014a,b; Descombes et al. 2014; Rogers et al. 2015). Satellite-based cloud advection methods can provide forecasts several hours out over a wide area but can experience difficulties with orographic clouds,

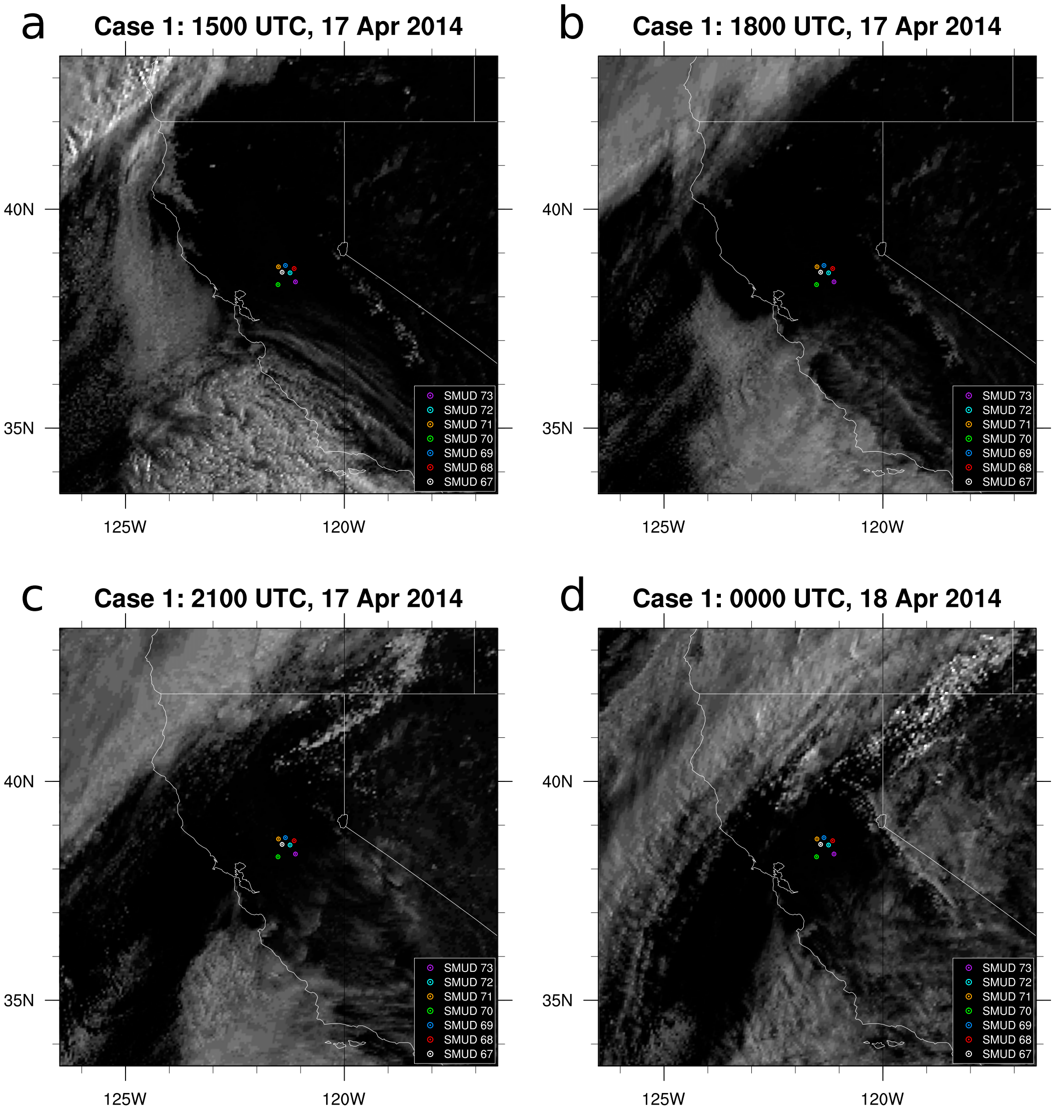

FIG. 2. *GOES-15* visible (0.65 μm) satellite imagery during case 1, at (a) 1500, (b) 1800, (c) 2100, and (d) 0000 UTC. The locations of SMUD sensors 67–73 are indicated by the colors in the legend.

marine-layer clouds in coastal zones, and other clouds that rapidly grow or dissipate after forecast initialization.

A fourth technique uses NWP model short-term cloud forecasts directly. NWP models can be applied for irradiance forecasting both on time horizons from minutes ahead, if properly initialized, to days ahead. NWP models generally provide accurate estimates of irradiance in clear-sky conditions, but skill decreases markedly in partly cloudy to cloudy conditions (e.g., Mathiesen and Kleissl 2011; Perez et al. 2013). This decrease in skill typically arises because of unresolved or poorly resolved clouds in the model, and thus overpredictions of GHI (Lara-Fanego et al. 2012). Improving predictions of subgrid-scale clouds can also have large impacts on cloud–radiation feedbacks, with a commensurate improvement to GHI predictions (Alapaty et al. 2012; Deng et al. 2014; Jiménez et al. 2016b). Aerosol–radiation feedbacks should also be accounted for to improve GHI forecasts from NWP models, particularly in clear-sky conditions (Ruiz-Arias et al. 2014; Jiménez et al. 2016a).

In this study, we examine several different solar irradiance forecasting techniques for four case days for the region surrounding Sacramento, California. These four case days represent typical cloud cover regimes of the region, and thus are a good test of GHI prediction systems. We compare 15-min average GHI predictions with observations from seven pyranometers owned and operated by the Sacramento Municipal Utility District (SMUD). A map indicating the locations of these pyranometers and nearby METAR sites appears as Fig. 1. Results indicate that each forecast system has its own strengths and weaknesses in the various regimes, times of day, and forecast lead times.

The paper is organized as follows. Section 2 describes the Sun4Cast forecasting system, the component models of which make up our forecast techniques. Section 3 briefly describes the four case days. Results are presented in section 4, and section 5 summarizes and concludes the study.

2. The Sun4Cast system

The Sun4Cast (there is a registered trademark application pending for this model) solar power forecasting system (Haupt 2013; Haupt et al. 2016; Haupt and Kosović 2016; Jiménez et al. 2016a) is composed of a nowcasting system that predicts 15-min average GHI out to 6 h and the Dynamic Integrated Forecast (DICast; DICast is a registered trademark) system (Mahoney et al. 2012) that blends NWP forecasts for hourly intervals out to 72 h. The aim of the system is to provide the most appropriate forecast technology for each time scale to accurately forecast power at particular solar installations. To do this requires leveraging both physical–dynamical models and artificial intelligence techniques. At the shortest time scales, the system employs data from TSIs to observe clouds from the ground and project their location over the following 15 min (TSICast) (Peng et al. 2015). StatCast (described below) blends surface pyranometer data with a variety of meteorological observations in generating artificial intelligence models to predict from 15 min out to 3 h. The version assessed here is StatCast-Cubist. The other nowcasting systems [the Cooperative Institute for Research in the Atmosphere Nowcast (CIRACast), the WRF-Solar Model, and the Multisensor Advection-Diffusion Nowcast (MADCast)] are described in more detail below and provide 15-min average forecasts out to 6 h. Beyond the nowcast horizon, the system leverages NWP forecasts from national centers, as well as local runs of the WRF-Solar system, to optimize the blend for each solar plant. The nowcast and DICast system forecasts are merged to provide seamless irradiance predictions. The system includes appropriate conversions between the GHI observed and the plane of array component of the irradiance that becomes the important component for most systems [although the concentrated solar plants utilize only the direct normal irradiance (DNI) component of the radiation].

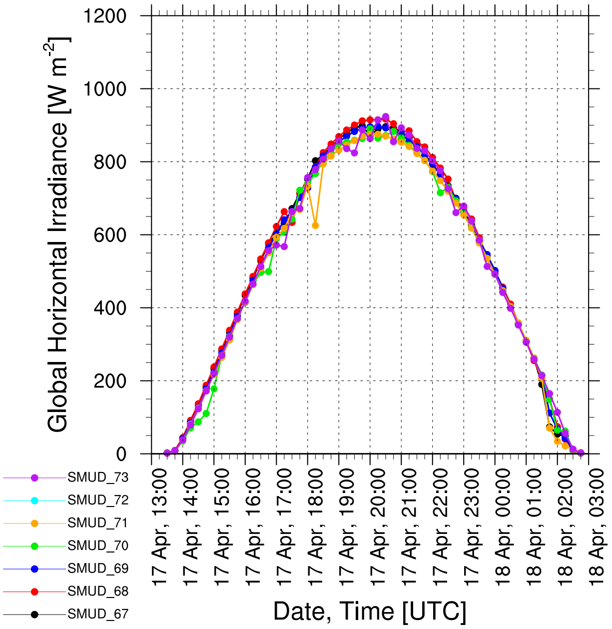

FIG. 3. Time series of 15-min-average GHI recorded by SMUD sensors 67–73 for case 1. The color for each sensor is indicated in the legend.

Once the irradiance forecast is finalized, it must be converted to power. The irradiance-to-power conversion

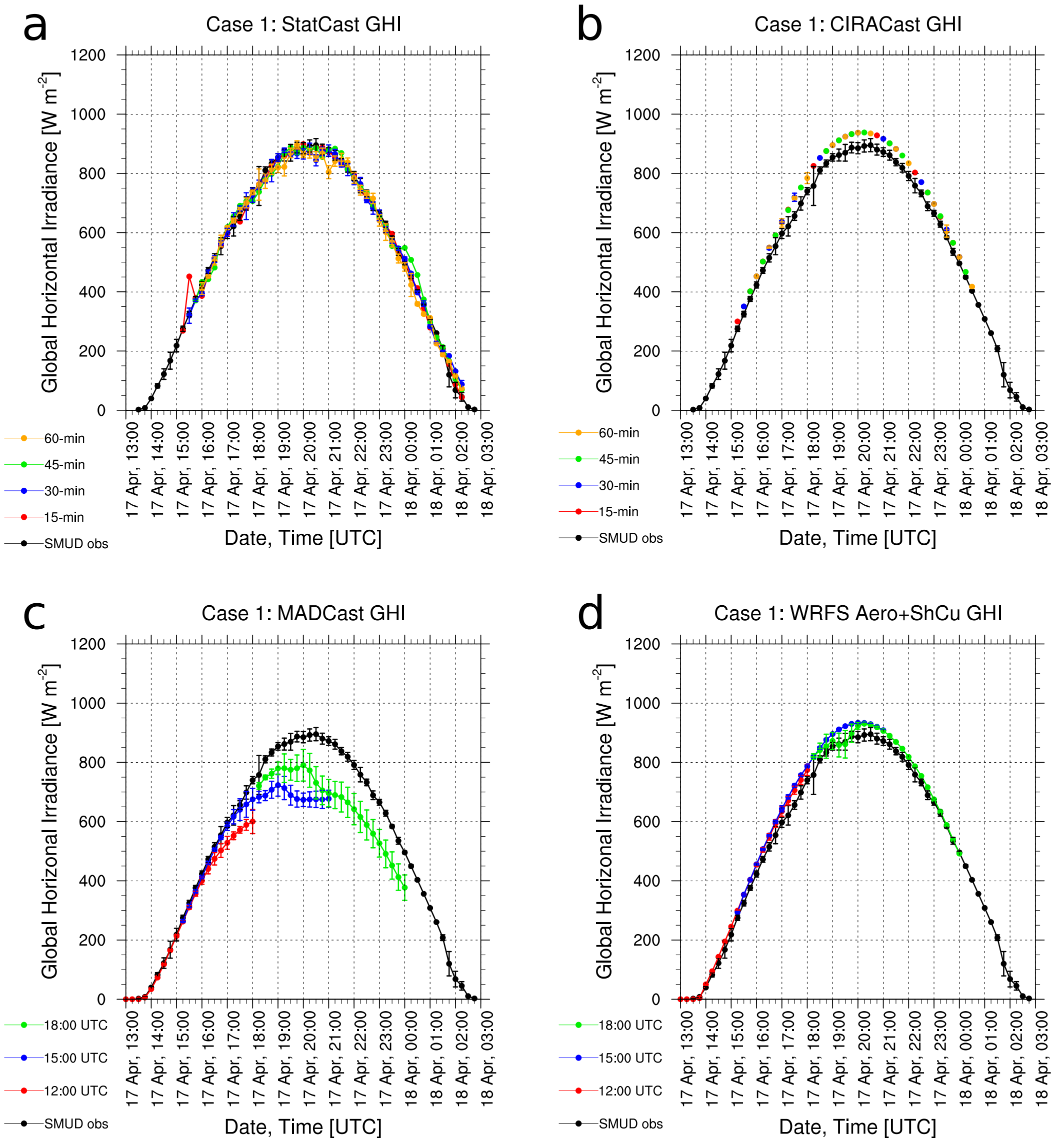

FIG. 4. The 15-min GHI predictions (colors) and observations (black) for case 1, averaged over the SMUD 67–73 sensors, for (a) StatCast, (b) CIRACast, (c) MADCast, and (d) WRF-Solar Aero+ShCu. The error bars for select time series denote ±1 std dev across the SMUD sensors.

algorithm consists of a machine learning model based on regression trees. The power forecast is further tuned using an analog ensemble (AnEn; Delle Monache et al. 2011, 2013; Alessandrini et al. 2015) approach that also provides uncertainty quantification, resulting in a tuned probabilistic forecast. The results are verified and validated with user-defined metrics and the power forecasts are translated to the end user at the utilities and ISOs to use in real-time decision-making. Our research team is working with those end users to assess the value of these probabilistic power forecasts. Because of the volume, variety, and complexity of the data involved, operationalizing the Sun4Cast system is a "big data" problem (Haupt and Kosović 2015, 2016).

a. StatCast-Cubist

McCandless et al. (2015) developed StatCast-Cubist as a technique to forecast short-term (0–3 h) irradiance at points where historical data are available. The artificial intelligence technique used for statistical short-range solar irradiance forecasting in StatCast-Cubist is the model tree, or Cubist model, which is the M5 model tree from Quinlan (1992) formatted as a set of rules (Kuhn et al. 2012). The model tree uses an algorithm to search for a rule that explains part of the training

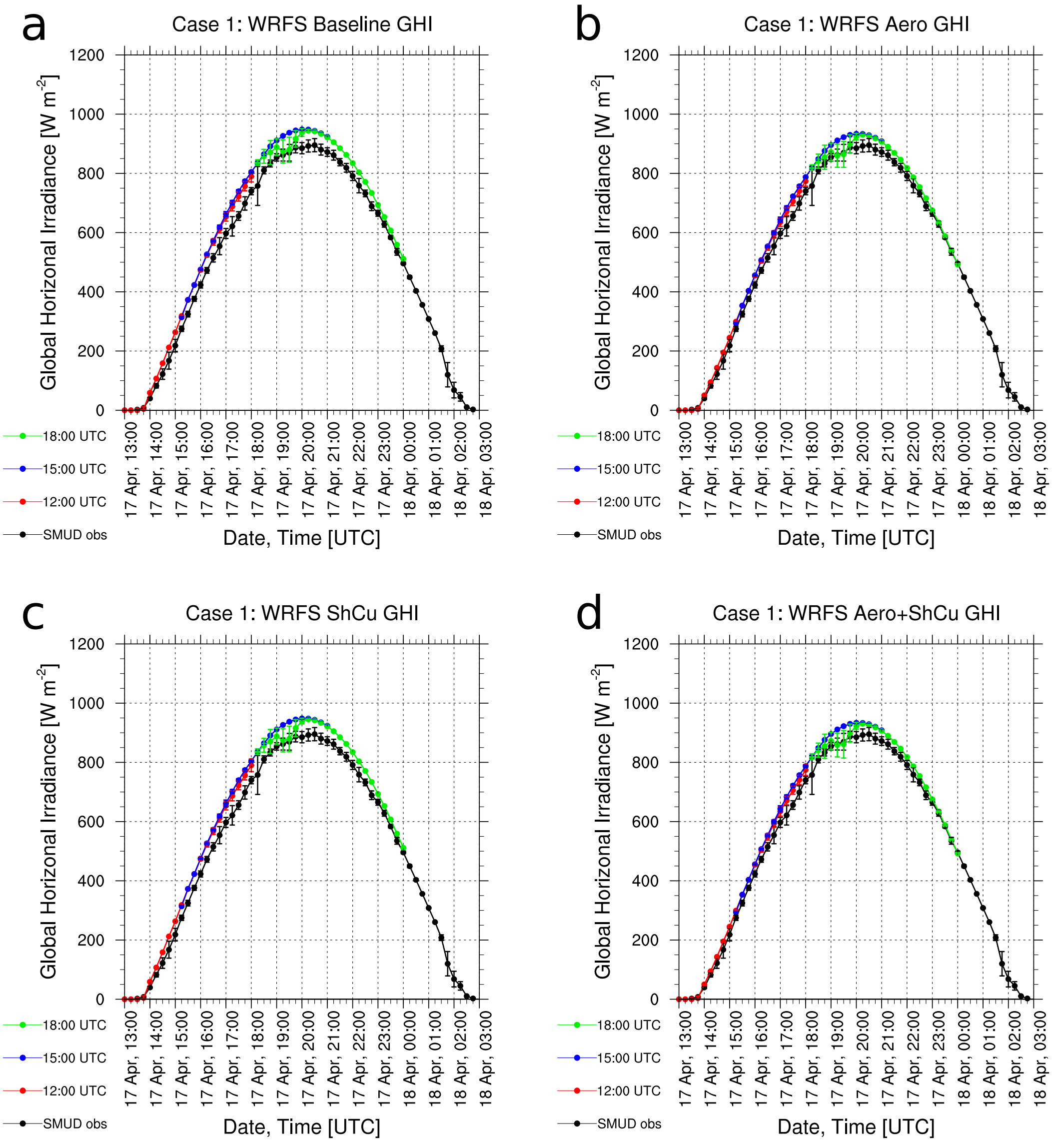

FIG. 5. As in Fig. 4, but for (a) WRF-Solar Baseline, (b) WRF-Solar Aero, (c) WRF-Solar ShCU, and (d) WRF-Solar Aero+ShCu.

instances, separates these instances, and continues this process until no instances remain (Quinlan 1996). The algorithm organizes the tree into a set of rules and defines a multivariate linear model at each leaf to predict the continuous GHI values. Quinlan (1987a,b, 1992) provides a detailed explanation of this process. The process “grows” a tree that includes multivariate linear regression models at its nodes and leaves. The final prediction is a weighted average of the multivariate linear regression equations at each node in the tree down to the final leaf (Kuhn et al. 2012). This weighted averaging is accomplished via a smoothing process that adjusts the predicted value from the leaf up to the root to capture the skill in the predicted values at nodes along the tree down to the final leaf, which prevents errors due to overfitting the training data.

The first step in implementing StatCast-Cubist was to build the dataset for training the model. The model required two sets of inputs: GHI observations from SMUD pyranometers and weather observations from the nearest METAR sites (KSAC, KSMF, and KMHR near Sacramento; see Fig. 1). One hour of 1-min-resolution irradiance observations from the SMUD observational network were averaged into four 15-min intervals leading up to the forecast initialization time. METAR observations for the most recent available observations (i.e., the hour preceding forecast initialization) were required for the three observational sites nearest to the point forecast

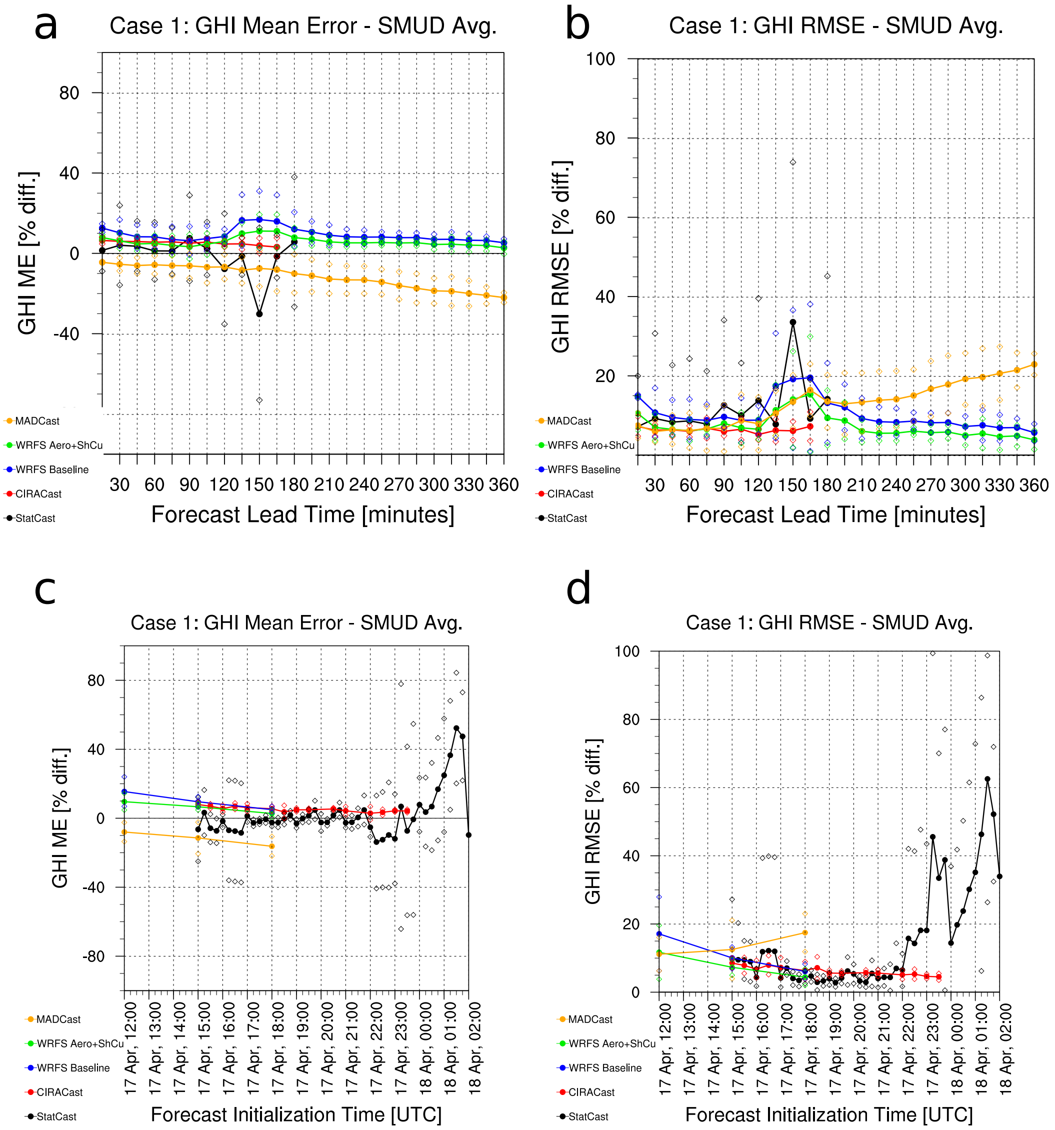

FIG. 6. Normalized (a),(c) MEs and (b),(d) RMSEs for case 1, as a function of (top) forecast lead time and (bottom) initialization time. Errors were calculated only when the SMUD network-average GHI was at least 50 W m^{-2}. Open diamonds denote the ±1 std dev range. Colors are described in the legends.

location. The weather variables used were temperature, dewpoint temperature, cloud cover, categorical precipitation (0 or 1), observed precipitation amount, and wind speed, which were selected to quantify the atmospheric state of the region at the time of the forecast. Additionally, the hour of the day (UTC) and yearday were inputs to the model, allowing the algorithm to model any seasonal and daily patterns.

The StatCast-Cubist model was trained with tenfold cross-validation on data for all daylight hours (i.e., both METARs and GHI observations >25 W m^{-2} at forecast initialization time) for the period from 25 January to 28 May 2014, excluding the four case study days. We trained 12 individual StatCast-Cubist models independently to predict each of the 12 forecast lead times from 15 min out to 180 min. Each of the 12 models had the same predictors, but each model had different predictands, with each model's predictands being historical GHI observations at one of the 12 specified forecast lead times. This training configuration allowed the StatCast-Cubist model to correct for any inherent systematic biases for those lead times.

b. CIRACast

The CIRACast forecast algorithm (Miller et al. 2012; Rogers et al. 2015) offers a satellite-derived short-term

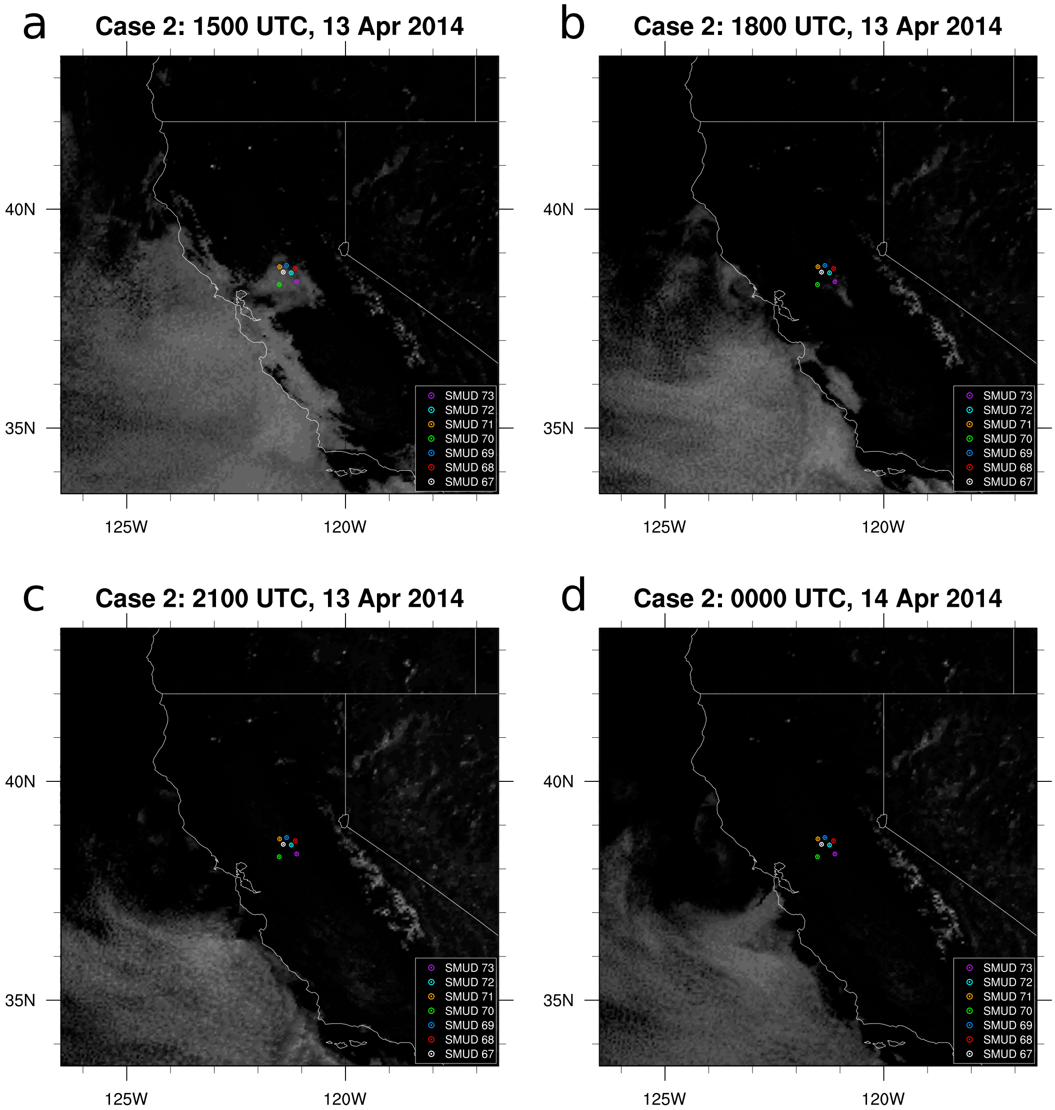

FIG. 7. As in Fig. 2, but for case 2.

prediction of GHI on a time scale of 5 min, providing forecasted GHI from the initial observation period out to 3 h from the time of observation. The method utilizes satellite retrievals of cloud-top properties derived from the NOAA Pathfinder Atmospheres–Extended (PATMOS-x; Heidinger et al. 2014) with an account for satellite viewing parallax displacements and 3D shadow casting for the current solar geometry. To yield a 15-min average GHI prediction, the arithmetic mean of three consecutive GHI forecasts covering the 15-min period of interest is calculated.

The CIRACast algorithm is predicated on the satellite-observed cloud field being projected forward in time using steering winds interpolated in space and time from NWP output. Retrieved cloud properties, including cloud-top height, cloud optical depth, and other physical properties taken from the PATMOS-x retrieval suite are used in the context of a similarity matrix (Rogers et al. 2015) to identify pixels belonging to unique cloud features using empirically determined similarity functions (Table 1). Placing these similar pixels into unique cloud groups, the identified cloud features are then advected forward in time using the centroid of each cloud group, and the identified cloud-top height for that centroid as the corresponding steering wind level from NWP guidance. Group trajectories utilize wind guidance interpolated in time from successive forecast periods within the NWP guidance rather than relying on a single, "frozen" vector taken from the initial NWP wind vector. As cloud groups are advected forward in time, the cloud properties for each group at each time step are saved as input data for a standalone version of the Satellite Algorithm for Surface Radiation Budget (SASRAB) radiative transfer code (Pinker and Laszlo 1992) employed within PATMOS-x to compute surface irradiance; specifically, cloud properties such as cloud-top height and cloud-cleared surface reflectivity (from a running two-week average from satellite observations) are used to account for parallax (a function of satellite viewing geometry and cloud-top height) and cloud shadow information (computed from sun angle and cloud-top height information) along with changes in steering wind velocity taken from the NWP guidance. The resulting calculations of GHI, DNI, and diffuse irradiance are then mapped to the original surface grid, allowing for direct forecasting as well as ingestion into the Sun4Cast system.

Observations from GOES-West and GOES-East are ingested, utilizing the conterminous United States (CONUS) scans from each satellite to define a forecast "box" large enough to contain the forecast locations and a sufficient area surrounding the locations to allow for several hours of translation within the advective scheme. Forecast lag time for each run amounted to approximately 15 min from the beginning of the satellite scan to the final advection-derived forecast.

c. MADCast

MADCast is a new model designed for the analysis and short-term forecasting of clouds (Auligné 2014a,b; Descombes et al. 2014). The cloud analysis is based on retrievals of multiple infrared sensors using the multivariate minimum residual (MMR) scheme (Auligné 2014a,b). MMR is implemented in the Gridpoint Statistical Interpolation analysis system (GSI; Kleist et al. 2009) and provides three-dimensional cloud fields. These cloud fields are used to initialize a modified version of the WRF Model (Skamarock et al. 2008). The model runs with simplified physics that allows for the faster speeds necessary to meet the needs of nowcasting applications. Finally, the predicted cloud field is used to diagnose the surface irradiance, completing the short-term forecast. The interested reader is referred to Descombes et al. (2014) for a complete description of this nowcasting component.

MADCast simulated the cloud field in a 9-km grid over the CONUS. The initial and boundary conditions were provided by the Rapid Refresh (RAP; Benjamin et al. 2016) analysis data from NCEP. The MADCast simulations are 6 h long with the lateral boundary conditions updated every 3 h. Three simulations were performed for each case study with the model initialized at 1200, 1500, and 1800 UTC. The model output was recorded every 15 min. The aerosol direct effect was represented using a 4° latitude × 5° longitude monthly climatology from Tegen et al. (1997), which is also the climatology used by the ECMWF global NWP model. Although MADCast is designed to assimilate irradiances from different satellite instruments, the forecasts herein presented only assimilated GOES-East irradiances [from channels 4 (10.7 μm) and 5 (12.0 μm), available at 30-min intervals] to analyze the potential of imagers on board geostationary satellites for solar irradiance forecasting.

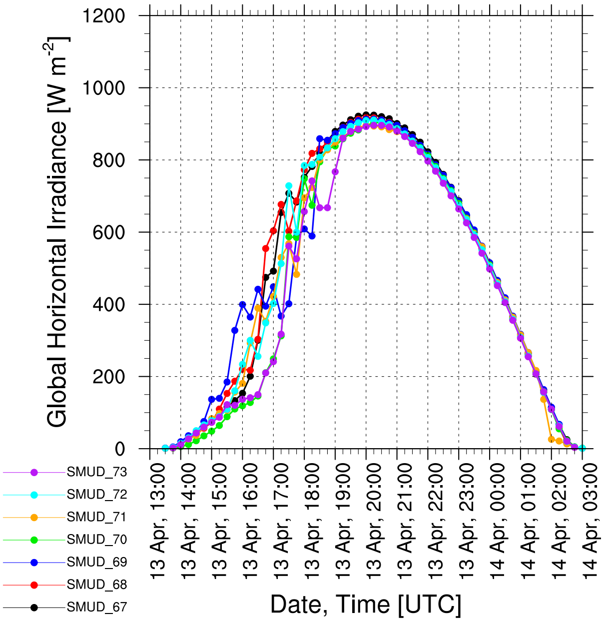

FIG. 8. As in Fig. 3, but for case 2.

d. WRF-Solar

WRF-Solar is a specific configuration of the WRF Model designed for solar energy applications (Jiménez et al. 2016a,b). Model developments include 1) developments to internally diagnose atmospheric variables for solar energy applications; 2) a flexible representation of aerosol–radiation feedbacks; 3) incorporation of cloud–aerosol feedbacks; and 4) enhanced representation of the cloud–radiation feedbacks, chiefly through the introduction of a new shallow cumulus parameterization scheme (Deng et al. 2014).

For these case studies, we ran four versions of WRF-Solar. The first experiment, "Baseline," only activated the solar augmentations introduced in support of solar energy applications, including an improved solar tracking algorithm and updates in the modeled surface irradiances at every time step of the model integration. The second experiment, "Aero," activated the aerosol direct

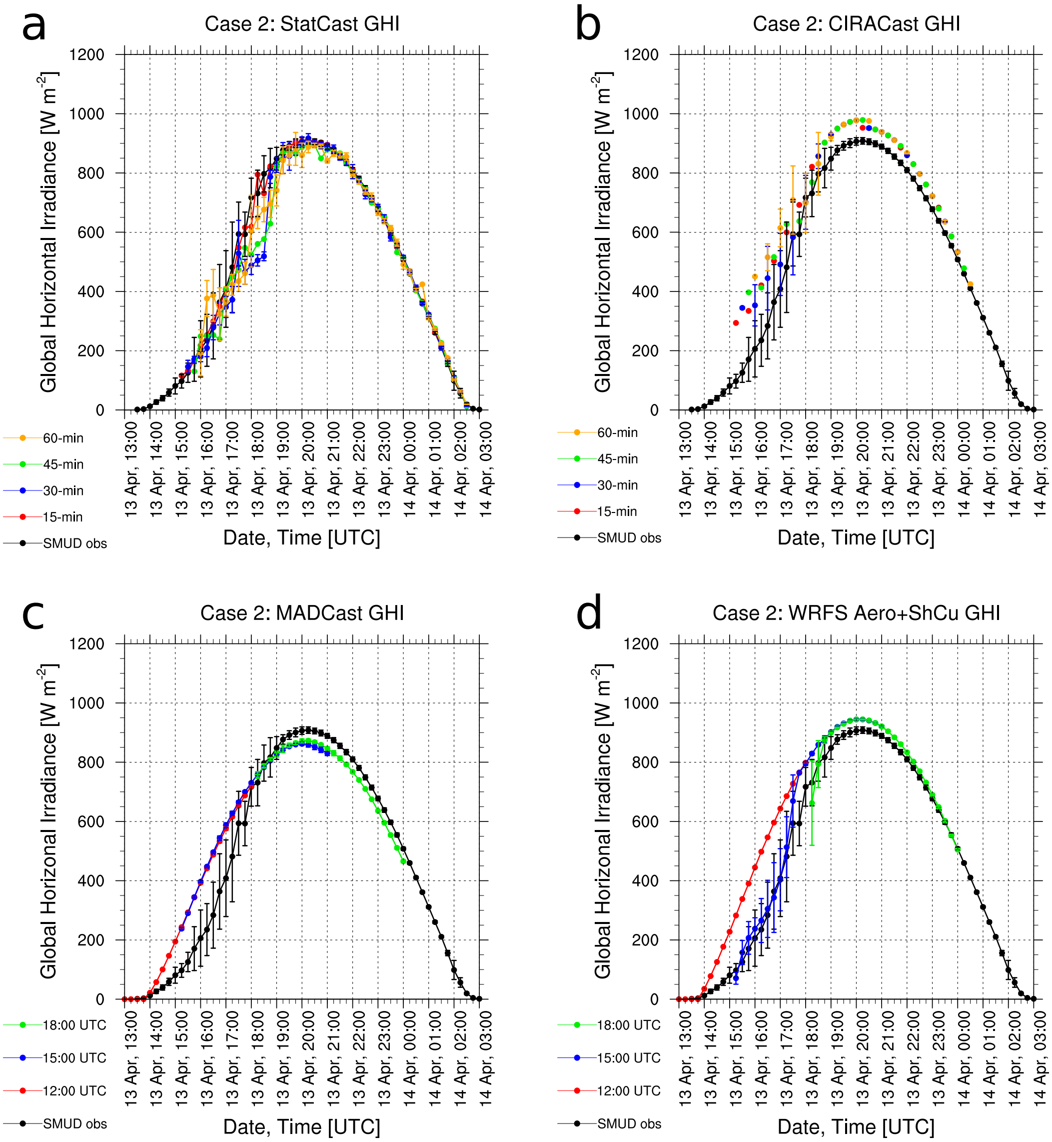

FIG. 9. As in Fig. 4, but for case 2.

effect using a high-resolution aerosol monthly climatology over CONUS (0.05° × 0.05°) generated from aerosol climatological data provided by Solar Consulting Services, as described in Jiménez et al. (2016a). The third WRF-Solar experiment, "ShCu," activated the Deng et al. (2014) shallow cumulus parameterization scheme to represent radiative effects of unresolved deep and shallow convective clouds (and thus, more precisely, it is a mass-flux parameterization scheme). The last WRF-Solar experiment, "Aero+ShCu," used both the higher-resolution climatological aerosol data and the Deng shallow cumulus scheme.

The four WRF-Solar experiments were run in an analogous way to the MADCast forecasts. The WRF domain had a horizontal grid spacing of 9 km over CONUS, and RAP analysis data were used as initial and boundary conditions of the 6-h simulations. The model was run three times per case study, initialized at 1200, 1500, and 1800 UTC, and the irradiances were recorded every 15 min.

3. Case descriptions

With the aid of archived METAR sky-cover observations from the Sacramento Executive Airport (KSAC) and *GOES-15*/GOES-West visible (0.65 μm) imagery, we identified four days in April 2014 that exhibited typical cloud cover regimes over the Sacramento

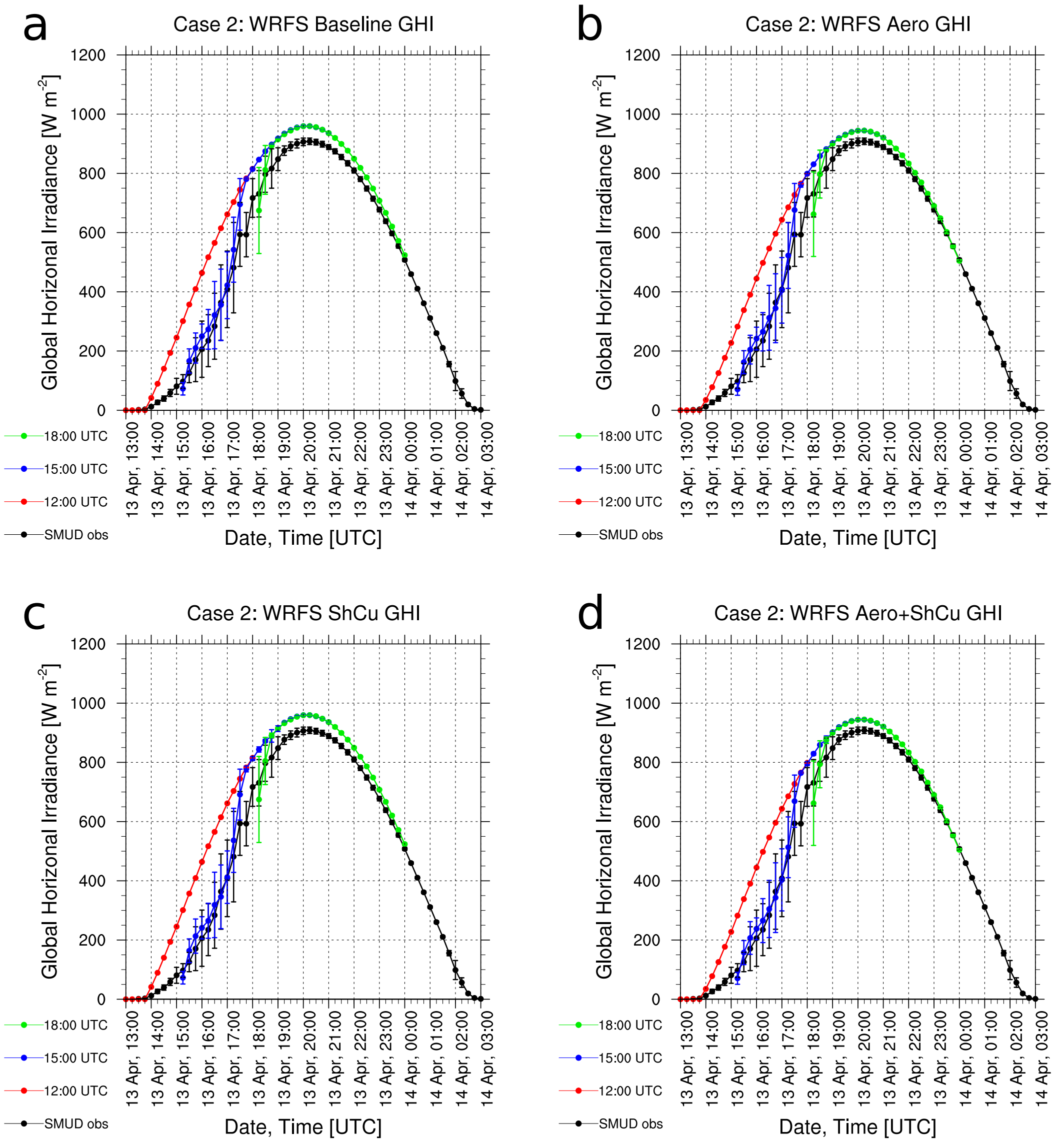

FIG. 10. As in Fig. 5, but for case 2.

area. Each of these four case days presents a unique challenge for models:

1) Case 1 (17 April 2014): This day had mostly clear skies around Sacramento, with only a few small, isolated clouds that briefly moved over individual SMUD pyranometers during the middle of the day. This is essentially a control case. Extensive cloud cover in northern and central/southern California made it a challenging clear day to model, however.
2) Case 2 (13 April 2014): This day had a low deck of marine stratocumulus in the Sacramento area in the morning. By about 1900 UTC [1200 Pacific daylight time (PDT)], the stratocumulus had burned off, leaving clear skies over each SMUD pyranometer. Predictions of the development, advection, and burn-off of marine stratocumulus clouds are challenging, and are of acute interest to utility operators on the West Coast.
3) Case 3 (22 April 2014): This day had mostly clear skies in the early morning, before a field of small cumulus clouds formed over the Sacramento area around 1800 UTC (1100 PDT). The mix of clouds and sun remained through sunset. This case is a challenging one for any model, as the field of fair-weather cumulus clouds was essentially stochastic.
4) Case 4 (25 April 2014): This day had mostly overcast, rainy conditions from sunrise to sunset, and 0.42 in. (10.67 mm) of rain fell at KSAC. From the *GOES-15*

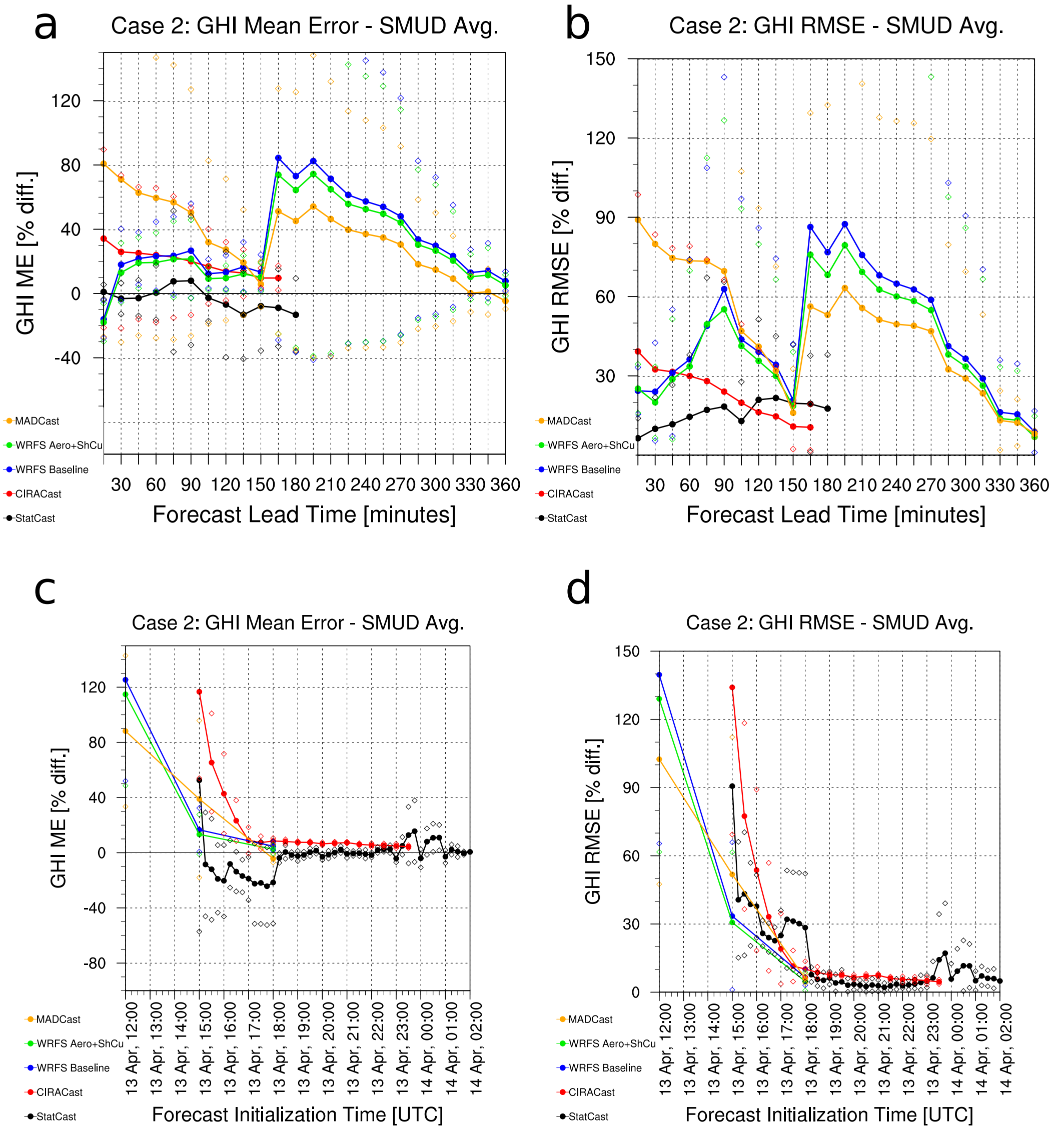

FIG. 11. As in Fig. 6, but for case 2.

imagery it was apparent that occasionally thinner clouds moved over some of the SMUD pyranometers throughout the day. This case is another tough test for the models.

The 550-nm aerosol optical depth (AOD) values from 1800 UTC (1100 PDT) on each case day near Sacramento are specified in Table 2. These data derive from the Modern-Era Retrospective Analysis for Research and Applications Aerosol Reanalysis (MERRAero) (Rienecker et al. 2011; Buchard et al. 2016). The 550-nm AOD values specified by the MERRAero dataset are similar to typical AOD values observed over several years in California's San Joaquin Valley (Lewis et al. 2010), so these are not abnormally clean or polluted–dusty days for the region.

4. Results

a. Case 1

Mostly clear skies dominated the Sacramento region sky conditions on 17 April 2014, though there was ample cloudiness to the northwest and to the south of Sacramento throughout the day, as seen in the four *GOES-15* (GOES-West) visible satellite images shown in Fig. 2, valid at 1500, 1800, 2100, and 0000 UTC. As the day progressed, clouds advanced toward Sacramento from both areas. The SMUD pyranometers in general also exhibited a clear-sky profile for GHI (Fig. 3), with little variability across the network. Network-averaged GHI observations and forecasts for the various models are

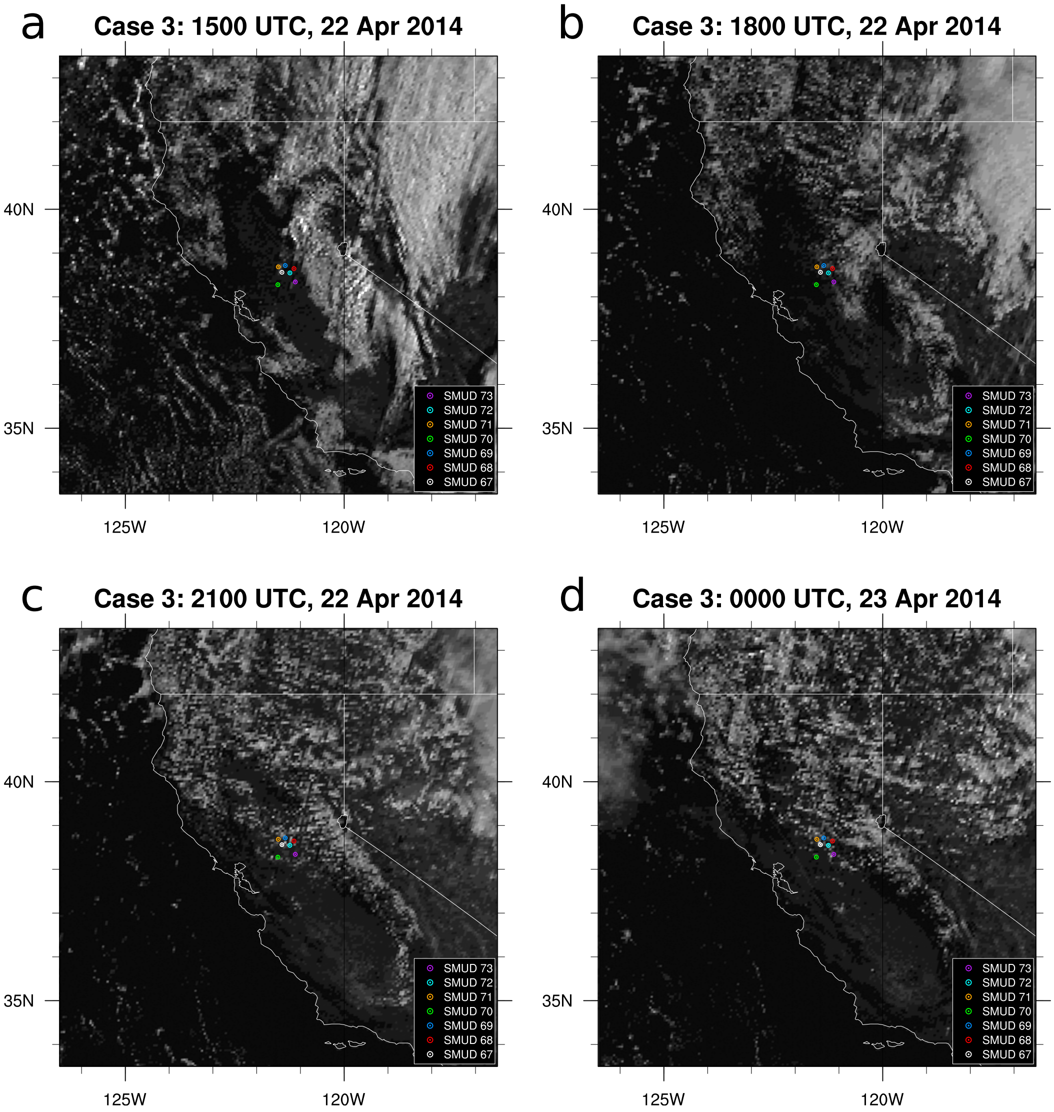

FIG. 12. As in Fig. 2, but for case 3.

shown in Figs. 4 and 5, and the network-averaged, normalized GHI mean (bias) errors (ME) and root-mean-square errors (RMSEs) as a function of both lead time and initialization time are found in Fig. 6. Normalized mean absolute errors (MAE) were also calculated, but they are not shown because they are quite similar to the RMSE figures and do not materially impact the interpretation of the results.

Note that in Figs. 4a,b, only the lead times out to 60 min for StatCast and CIRACast are presented to reduce clutter. The remaining panels (Figs. 4c,d and 5) show the three forecast initialization times (1200, 1500, and 1800 UTC) for MADCast and WRF-Solar. Error bars denoting ±1 standard deviation across the SMUD network are always displayed for the observations, but only for select forecast time series to reduce clutter. The WRF-Solar Aero+ShCu forecasts are shown in Figs. 4d and 5d to facilitate easier comparison among the various forecasts. Additionally, the open diamonds in all four panels of Fig. 6 denote a range of ±1 standard deviation in the normalized errors for each time series. Furthermore, the normalized errors were only calculated for the times at which the observed average GHI was $\geq 50\,\mathrm{W\,m^{-2}}$ to reduce contamination of the average scores by inflated normalized errors near sunrise and sunset, times at which little energy would be generated. The same plotted quantities, plotting conventions, and ranges are used for all the cases, except for the normalized errors plots, for which the plotted ranges change for each case.

Except for MADCast (Fig. 4c), all the forecasting systems performed well for this day. MADCast, after performing relatively well for the first few hours during the 1200 and 1500 UTC runs with average bias errors generally between −1% and −6% prior to midmorning, incorrectly predicted that some of the clouds in the region would reach the SMUD sites, thus attenuating the modeled GHI significantly and leading to substantial underforecasts of −10% to −25% from midmorning through the afternoon, and average bias errors of about −15% for the 1800 UTC run (Fig. 6c). This highlights a limitation of satellite-based techniques, though CIRACast (Fig. 4b), the other satellite-based technique here, did not suffer the same issues as MADCast. On the other hand, CIRACast displayed a small consistent overforecasting bias of generally around 4%–7% for all lead times and initialization times (Fig. 6). This positive GHI bias stems from the parameterized aerosol loading in CIRACast being insufficient for this case day.

This assumption is supported by the WRF-Solar experiments with the default aerosol modeling (Baseline and ShCu; Figs. 5a,c) having an even larger, consistent positive GHI bias than CIRACast of generally around 8%–15% for most lead times (the small bump in normalized errors around lead time 150 min is caused by the 1200 UTC run forecasting for shortly after sunrise, when observed GHI is relatively small). Meanwhile, the WRF-Solar experiments with a representation of the aerosol direct effect (Aero and Aero+ShCu; Figs. 5b,d) yielded a notably reduced positive GHI bias of around 5%–9% for most lead times. This is compelling evidence that improved handling of aerosols is necessary for numerical models to have better clear-sky GHI predictions, which is a finding consistent with Jiménez et al. (2016a).

The best-performing forecast model on this day was StatCast (Fig. 4a), which had a mean error from −1% to 4% for most lead times (Fig. 6a), and average mean errors from about −6% to +6% for most initialization times (Fig. 6c). Note that the StatCast errors for later initialization times increase markedly in Figs. 6c,d because of the forecasts heading into the evening, where small actual errors become much larger normalized errors because of low observed GHI. As StatCast was trained on actual GHI observations and weather conditions around the same time, it already accounts well for the aerosol loading in this region at this time. This result highlights one of the strengths of statistical forecasting; provided it is not significantly different from other days in the training dataset, no direct knowledge of the local aerosol loading for the current day is needed, and the observed irradiance on the current day forms an optimal basis for the prediction.

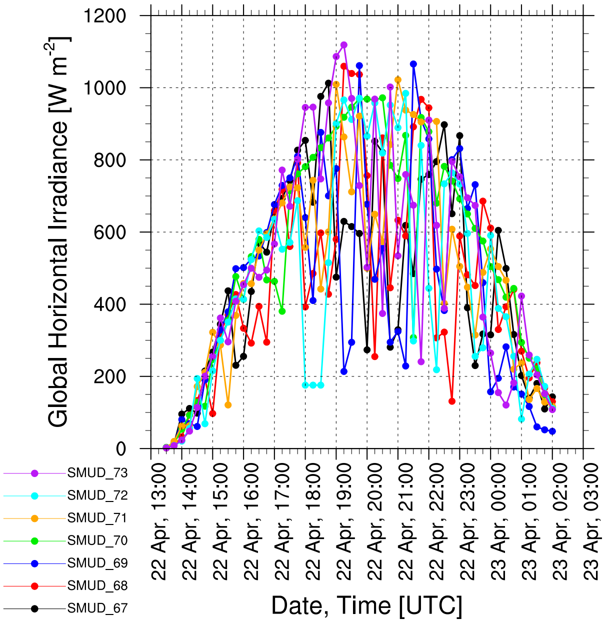

FIG. 13. As in Fig. 3, but for case 3.

b. *Case 2*

An area of marine stratocumulus clouds was widespread across coastal regions of California, and had infiltrated through the Golden Gate to the Central Valley around the SMUD region early in the morning of 13 April 2014, as seen in Fig. 7. The stratocumulus gradually burned off by about 1900 UTC, though not uniformly over all the sensors, and clear-sky conditions prevailed the rest of the day (Figs. 7 and 8). Network-average observations and forecasts are shown in Figs. 9 and 10, and normalized average GHI forecast errors as a function of lead time and initialization time are displayed in Fig. 11.

The first thing to note about the errors is that each of the forecast components had large average normalized errors in the first run of the day (Figs. 11c,d), primarily because of large relative errors in the very early morning. This also explains the large increase in normalized errors at lead time 165 min for MADCast and all WRF-Solar versions (Figs. 11a,b), as the observed GHI did not reach the 50 W m^{-2} threshold for calculating errors until 165 min after the 1200 UTC initialization time.

For the first 90–115 min of forecast lead time, StatCast unquestionably provided the best forecasts, as it had the lowest errors (Figs. 9a and 11). For these short lead times, not only did StatCast perform well during the cloudy morning, but also during the clear skies in the afternoon, as in case 1. Errors increased steadily at longer lead times, however, indicating that a longer training dataset would likely be helpful to capture

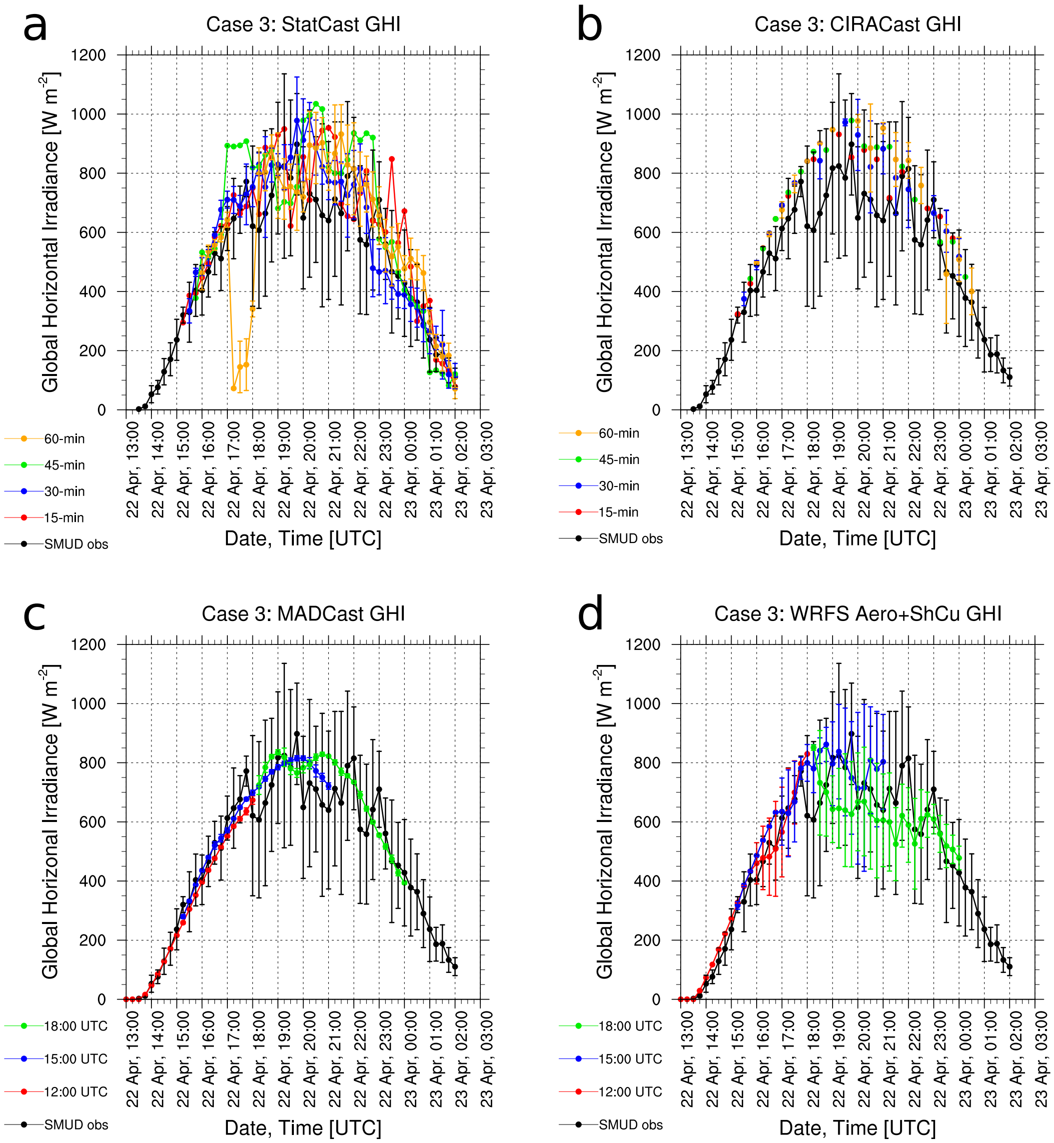

FIG. 14. As in Fig. 4, but for case 3.

additional marine-layer events similar to this one. Once the skies cleared by late morning, however, the StatCast forecasts were superb, with average bias errors near 0% for much of the rest of the day.

CIRACast forecasts for the early morning failed to capture the marine-layer clouds, but forecasts initialized later in the morning improved in predicting the cloud-attenuated GHI for 15–45-min lead times (Fig. 9b). This short-term improvement for midmorning was likely due to improved identification of the cloud objects on the visible satellite data owing to a higher sun angle. However, even when CIRACast identified the presence of clouds in the SMUD area at initialization, CIRACast appeared to advect these stationary clouds out of the area after about an hour, thereby returning GHI forecasts to near clear-sky values. Correctly simulating stationary or terrain-locked clouds remains a difficult problem for satellite-based forecasts. For the clear skies later in the day, CIRACast suffered from the same positive GHI biases that occurred during case 1, but otherwise performed well, with ME and RMSE generally <10% for all forecasts initialized after midmorning (Figs. 11c,d).

MADCast, like CIRACast, predicted insufficient cloudiness in the morning over the SMUD region, and so overforecasted GHI in the morning (Fig. 9c). In the clear-sky conditions, however, MADCast had a negative GHI bias, unlike any of the other models. This can likely

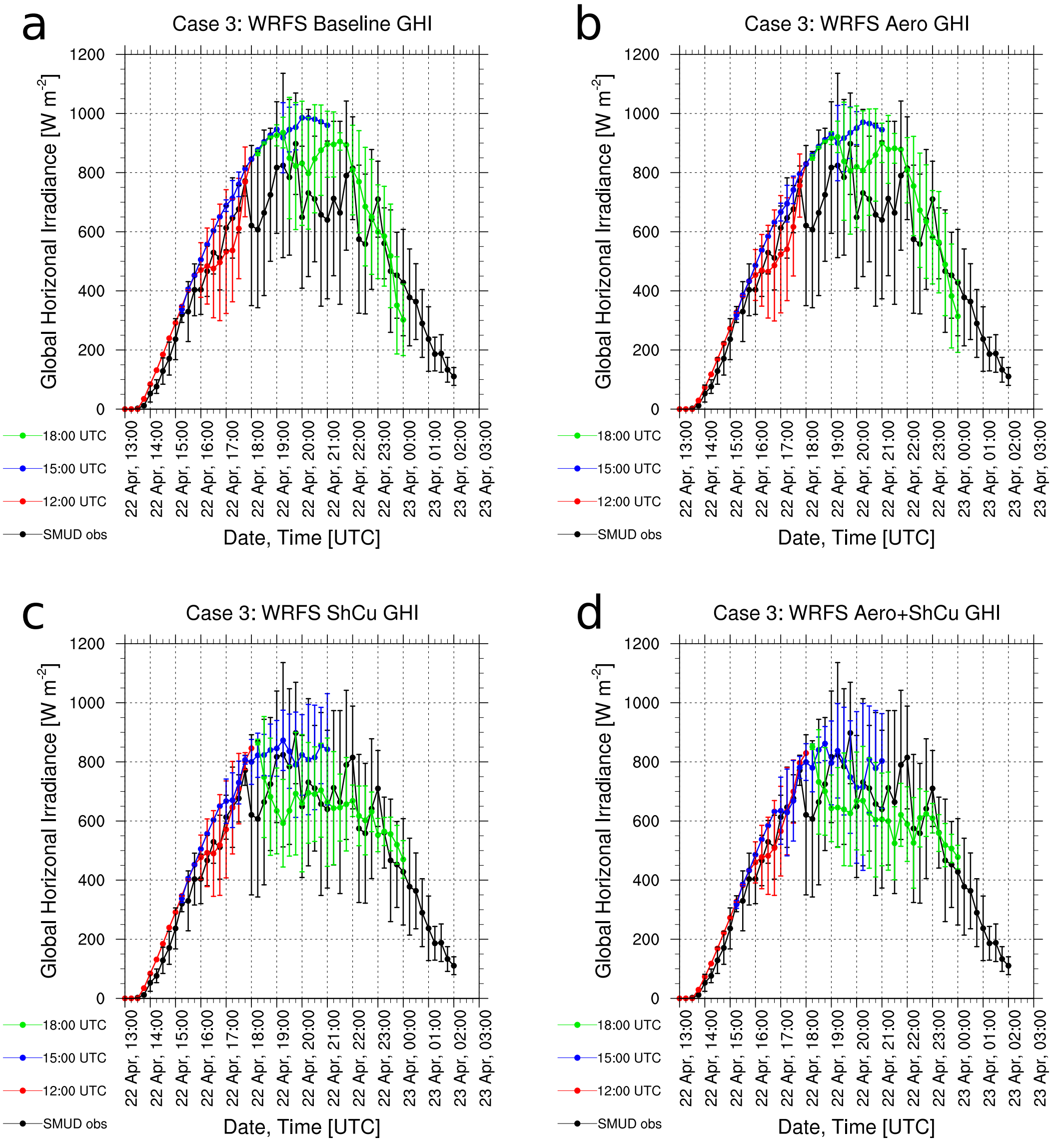

FIG. 15. As in Fig. 5, but for case 3.

be primarily attributed to MADCast diffusing and advecting marine stratocumulus from the northern California coast to the Sacramento area, thereby providing a thin cloud cover in the model over the SMUD sensors, instead of dissipating the largely stationary clouds by about midday as was observed. This finding illustrates that satellite-based methods like MADCast simply cannot capture formation or dissipation of clouds after forecast initialization and can also sometimes struggle handling orographic or other semistationary cloud features. And yet, despite these flaws in the forecast, MADCast had lower errors on average than any of the WRF-Solar versions for lead times of 150 min and beyond (Figs. 11a,b).

For the WRF-Solar experiments, none of the 1200 UTC runs simulated any clouds, while the 1500 UTC runs all nearly perfectly handled the marine layer for most of the morning, except for burning off the stratocumulus about 1–2 h too soon (Fig. 10). The 1800 UTC runs burned off the clouds at nearly the correct time. These findings illustrate the tremendous potential value that NWP can have in tricky forecast situations, even for nowcasting time scales, though additional work is needed to identify why the 1200 UTC runs failed to capture the marine-layer clouds entirely. For the clear skies later in the day, WRF-Solar forecasts exhibited similar positive GHI biases that were endemic to the case-1 forecasts, with reduced biases

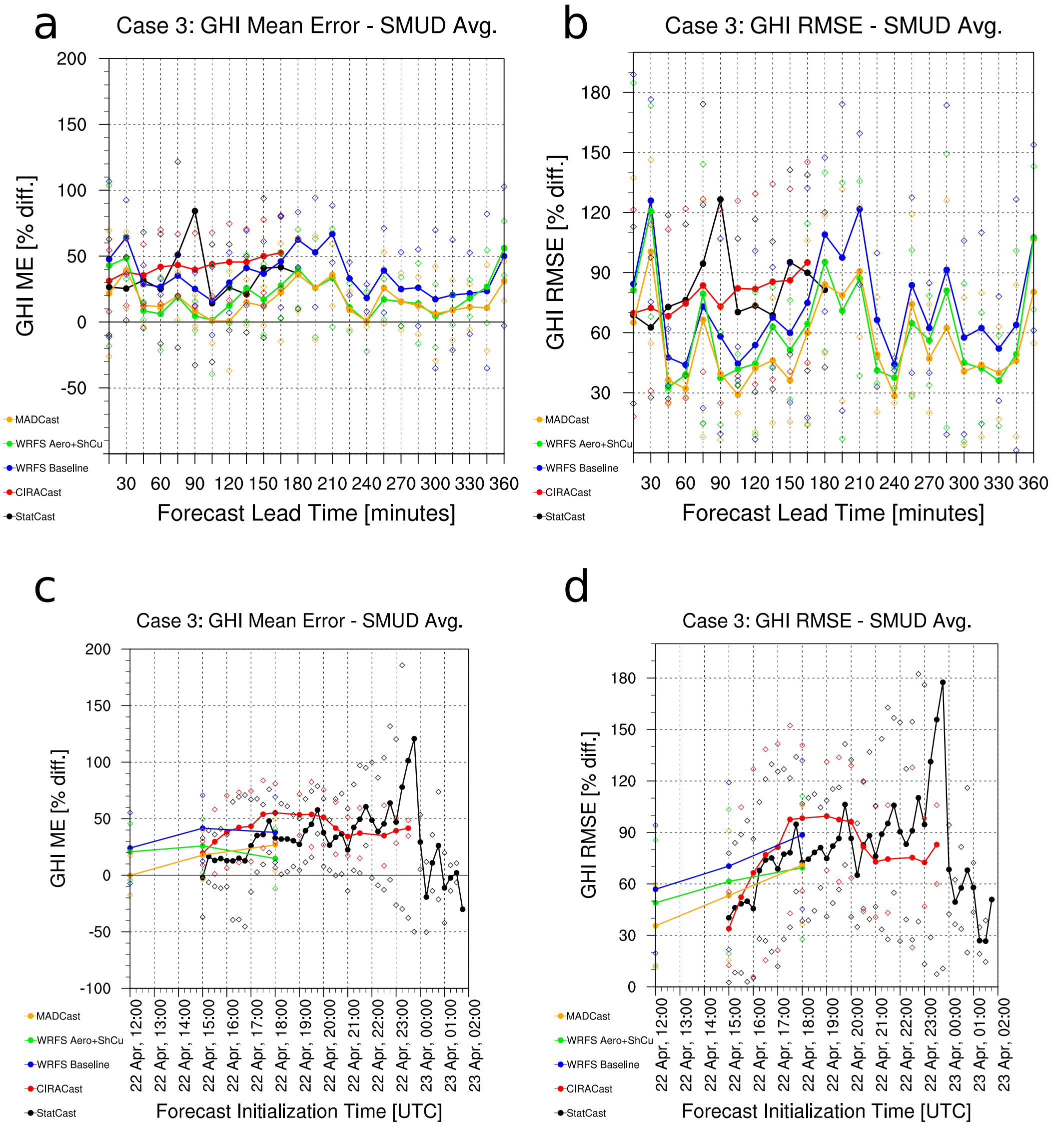

FIG. 16. As in Fig. 6, but for case 3.

in the Aero and Aero+ShCu experiments (Figs. 10b,d) relative to the Baseline and ShCu experiments (Figs. 10a,c).

c. *Case 3*

Case 3 is a particularly interesting and challenging case to model because a widespread and long-lasting field of fair-weather cumulus formed in place over the SMUD region by about 1800 UTC on 22 April 2014, after clear skies were present in the morning (Fig. 12). The immense variability in observed GHI across the SMUD network throughout the day can be seen in Fig. 13. For a situation like this, correct predictions of the extreme variability in the forecast across the network would be critical to grid operators. GHI forecasts and observations for StatCast, CIRACast, MADCast, and WRF-Solar are shown in Figs. 14 and 15. Normalized forecast errors as a function of lead time and initialization time appear in Fig. 16.

Figures 14 and 15 indicate that all of the forecast methods actually performed reasonably well for this complex and difficult case, though StatCast (Fig. 14a) and CIRACast (Fig. 14b) generally had an average positive GHI bias of 25%–40% through the first 60 min of lead time. Later lead times generally had even larger errors for this case (Fig. 16), which is to be expected in general, and especially for a case with a highly variable cloud field that forms in place overhead more or less

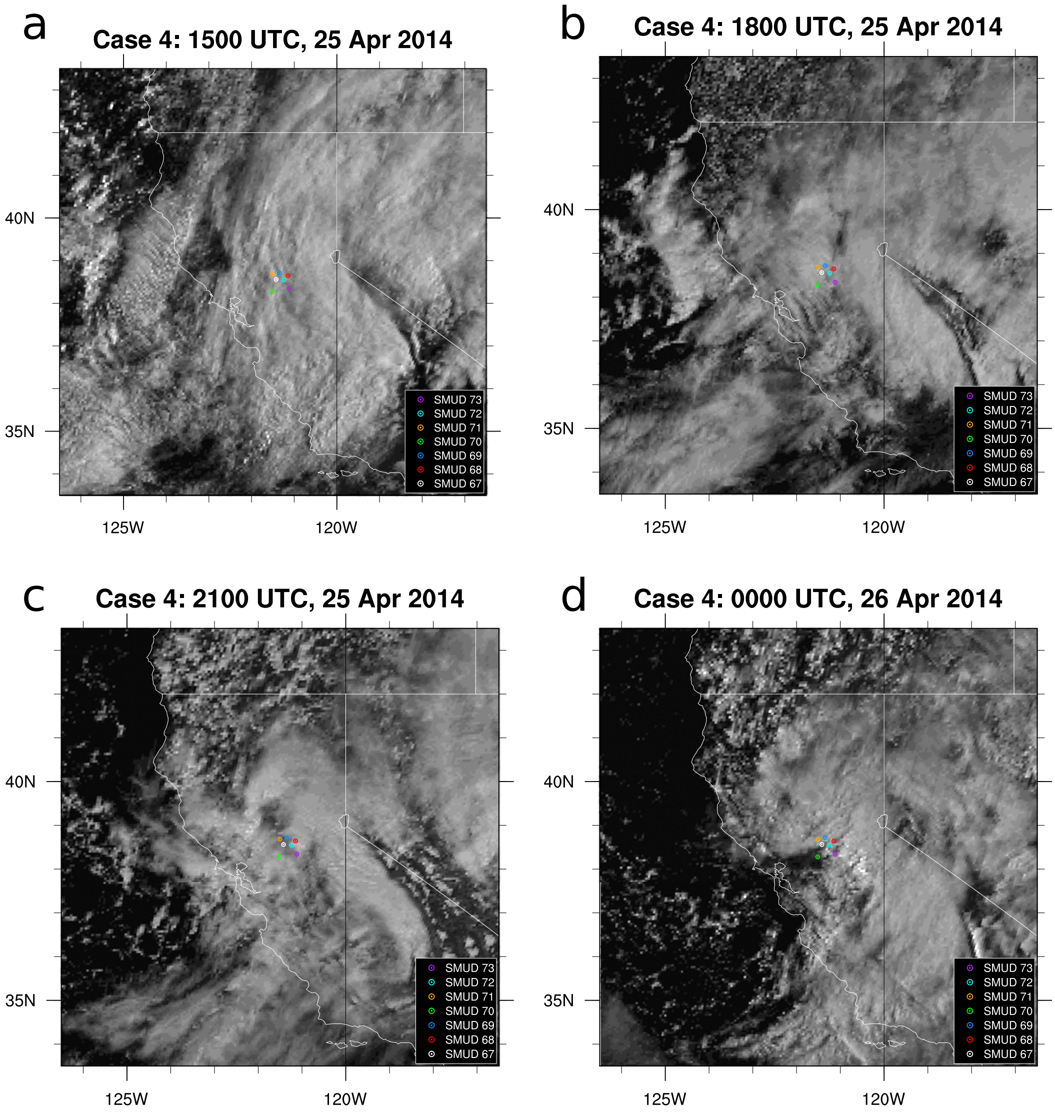

FIG. 17. As in Fig. 2, but for case 4.

stochastically, rather than being advected into the area. Cases like this are inherently difficult if not impossible for satellite-based forecasting systems like CIRACast to capture well.

MADCast, somewhat surprisingly, generally had the lowest errors overall of any of the forecast modules for case 3 (Fig. 16), with average bias errors ranging from 0%–30% for most lead times, because its SMUD-average predictions remained in the middle of the variability (Fig. 14c). The small error bars on the MADCast predictions are indicative of a smooth cloud field that was consistent over the entire network at any given time. So even though the details of the cloud field were incorrect in MADCast, and even though the variability was grossly underpredicted, the average GHI prediction was, on balance, relatively good for this particular day.

The WRF-Solar runs with the Deng ShCu scheme turned on (ShCu and Aero+ShCu, Figs. 15c,d) also had generally improved errors relative to the runs without the ShCu scheme (Baseline and Aero, Figs. 15a,b), illustrating the benefits of using that scheme to better represent unresolved clouds. The underprediction of low clouds in the Baseline and Aero simulations is consistent with results from both Cintineo et al. (2014) and Arbizu-Barrena et al. (2015), which found that WRF tends to underpredict low-level clouds in particular, regardless of microphysics or boundary layer parameterization scheme. The WRF-Solar ShCu and Aero+ShCu versions had error statistics that were quite competitive with and sometimes better than

MADCast for this case, with mean errors generally less than 30% on this challenging day (Fig. 16).

d. Case 4

Skies were overcast throughout 25 April 2014, but not uniformly overcast, as can be seen in the satellite images in Fig. 17 every 3 h from 1500 to 0000 UTC. The occasional thinning of the clouds over certain sensors was reflected in the occasional peaks in observed GHI in Fig. 18, though observed GHI was quite low most of the day. GHI forecasts from the various models are shown in Figs. 19 and 20, with the normalized forecast errors as a function of lead time and initialization time displayed in Fig. 21.

StatCast predictions were, on average, generally the best out to a lead time of 45 min (Fig. 19a), but the errors grew quickly beyond that lead time (Figs. 21a,b). The short positive trends in GHI as clouds occasionally thinned appear to have led to StatCast predicting those thinning trends to continue in many instances, leading to large errors of >150% at longer lead times. Overcast days are far less common in Sacramento than clear days, but a longer training dataset with additional overcast days included would likely have led to better StatCast forecasts.

CIRACast predictions initialized early in the morning (up to 1600 UTC) were among the best forecasts on this day (Figs. 21c,d). At short lead times (<60 min) CIRACast was also reasonably competitive with the other models (Figs. 21a,b), but with a marked positive GHI bias indicating that the clouds were not optically thick enough in the model, and occasional near-clear-sky forecasts for short periods (Fig. 19b). Errors in the GHI forecast from CIRACast also grew with time; at lead times beyond 90 min, the errors were generally the largest of any of the models. The satellite loop for that day revealed pockets of clear sky or thin clouds to the west of Sacramento periodically, which eventually were filled in by other, thicker clouds before reaching the Sacramento area. It is these clear pockets that CIRACast detected and predicted would advect over the SMUD region. As with case 3, satellite-based forecast methods have extreme difficulty performing well when the cloud field rapidly develops or dissipates after initialization.

MADCast did predict cloud cover, and the analyses at the initial time were not bad, but, like CIRACast, the cloud cover was not optically thick enough (Fig. 19c). Also, as in case 3, the variability in the MADCast forecasts was generally far smaller than the observed variability, and far smaller than the CIRACast variability. Even so, it was one of the better forecasts on this day, from an average error standpoint, though the errors did grow steadily with lead time (Figs. 21a,b).

The WRF-Solar forecasts without the Deng scheme (Baseline and Aero, Figs. 20a,b) did a poor job simulating the clouds through most of the day. Positive GHI biases were often large because of insufficient cloud coverage and thickness, and the average errors were frequently the largest of any model, with average bias errors often exceeding 200% (Fig. 21). As with case 3, this result is consistent with the general underprediction of low-level cloudiness in WRF that was found by Cintineo et al. (2014) and Arbizu-Barrena et al. (2015). On the other hand, in the experiments with the Deng shallow cumulus scheme (ShCu and Aero+ShCu, Figs. 20c,d), the GHI biases were markedly reduced and even nearly eliminated during the middle of the day. These experiments generally produced the lowest errors of any model for case 4, with average bias errors under 75% for the 1500 and 1800 UTC runs (Fig. 21c). Even more so than case 3, these results for case 4 highlight the vital importance of simulating unresolved clouds for obtaining good GHI forecasts.

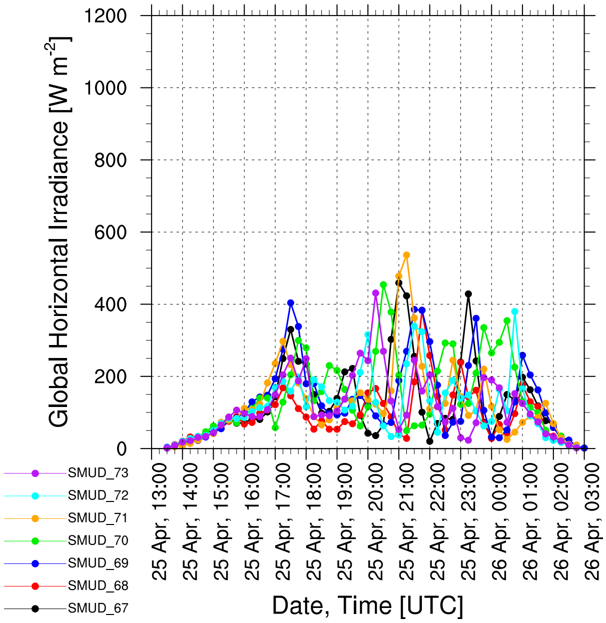

FIG. 18. As in Fig. 3, but for case 4.

5. Summary and conclusions

In this study, we compared the GHI forecasts from several forecast models—StatCast, CIRACast, MADCast, and four versions of WRF-Solar—over four case days with canonical sky-cover regimes for the region of Sacramento, California. We compared the various forecasts with observations from seven pyranometers operated by the Sacramento Municipal Utility District. The four case days included a clear-sky day, a day with morning marine-layer stratocumulus followed by clear sky, a day

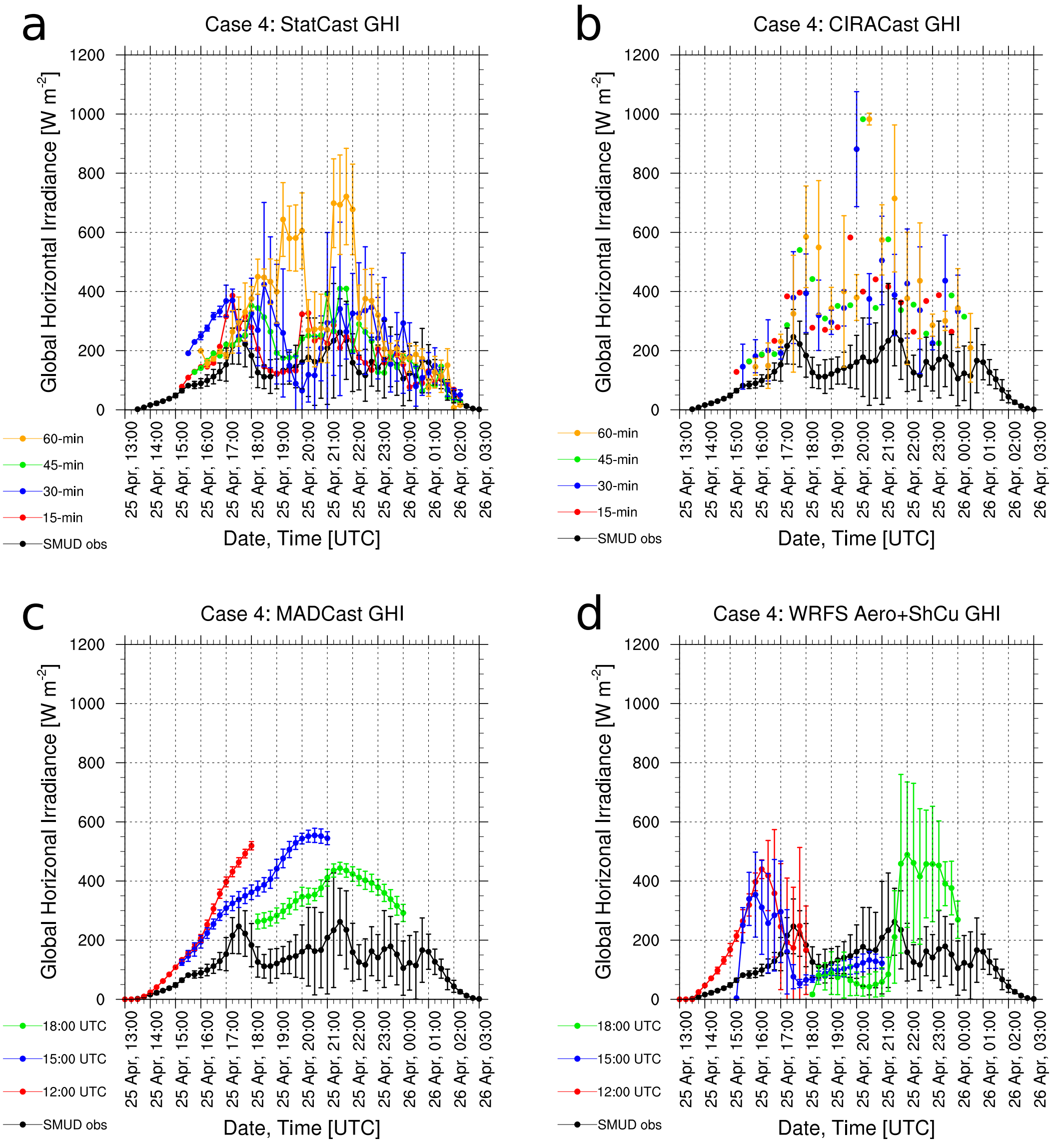

FIG. 19. As in Fig. 4, but for case 4.

with a field of fair-weather cumulus forming in place over the region, and an overcast day.

Statistical forecasting, as accomplished with StatCast-Cubist, was the best forecast when skies were clear, with bias errors generally <5%, because its training dataset and the observations on that day had already accounted for attenuation from typical aerosol loading in the area. Furthermore, there was an abundance of clear days in the training dataset (64% of the days in the training dataset had clear skies throughout the daytime period at KSAC), which benefitted StatCast's performance for case 1. For all case days, StatCast also had some of the lowest errors in the first 45–60 min. When clouds were present, however, GHI forecast errors for longer lead times increased, unsurprisingly, especially in cases when trends in GHI reversed themselves due to rapidly changing cloud cover overhead.

Satellite-based forecasting, as with CIRACast and MADCast, was also generally good at short lead times in comparison with the other models but struggled on days when clouds were rapidly forming, growing, and decaying after forecast initialization. These types of situations are a major limitation for satellite-based forecast models. MADCast generally predicts a smoother, more diffuse cloud field than does CIRACast, which sometimes resulted in better mean GHI predictions across the network for MADCast, but at the cost of grossly underestimating the GHI variability. On

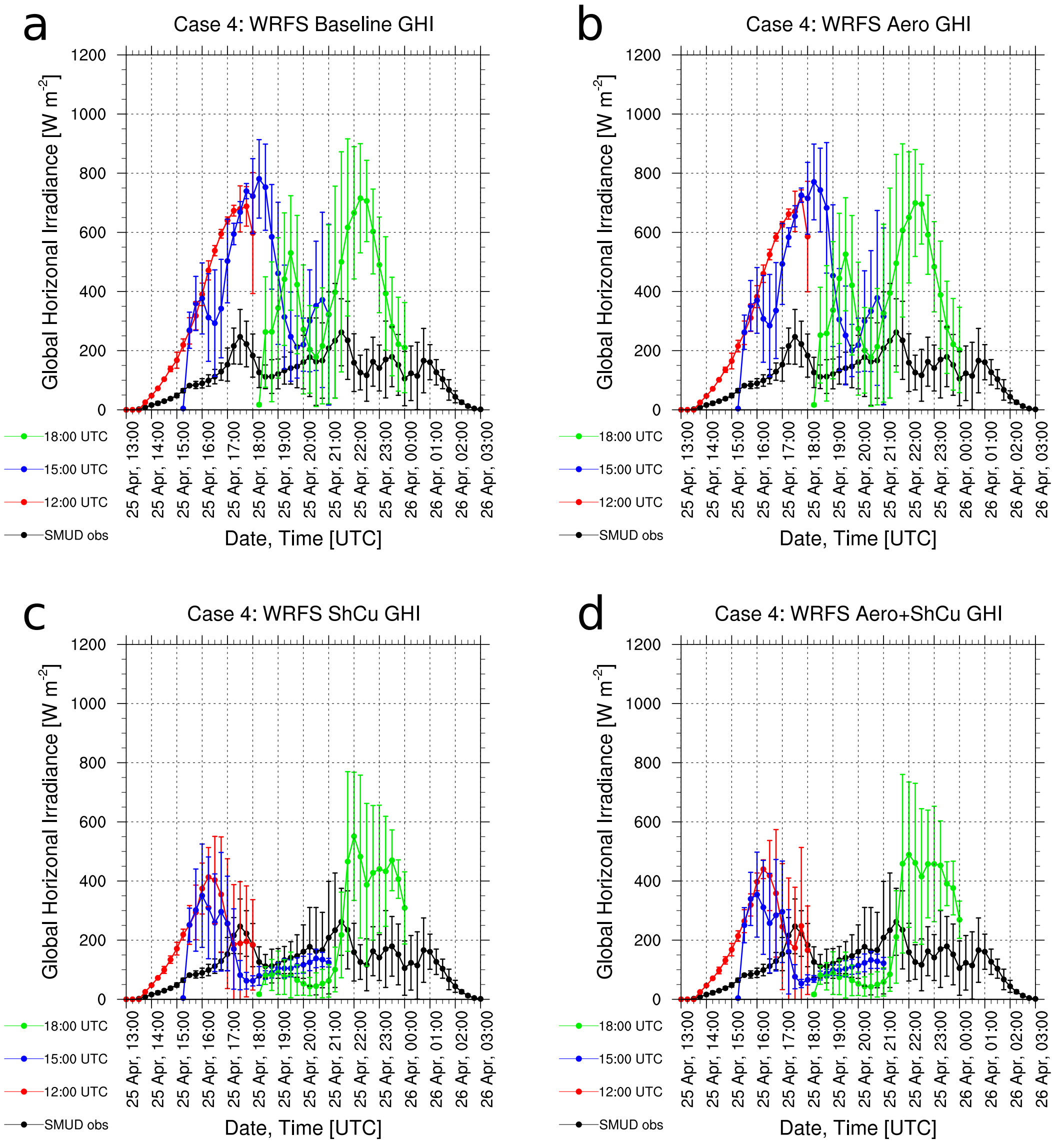

FIG. 20. As in Fig. 5, but for case 4.

the clear afternoon of case 2, CIRACast had a positive GHI bias of a little under 10% because it predicted clear skies, while MADCast had a negative GHI bias of about −5% because it advected some thin marine stratocumulus clouds from the coast, even though the observed clouds were mostly stationary and dissipated. For models that either assimilate or identify cloud features and then advect those clouds, without including any other cloud physics in the model, details of how to handle nearly stationary or terrain-locked clouds are a vital consideration in many locations.

Numerical weather prediction with WRF-Solar was shown to provide rather accurate GHI predictions for all the cases studied here, especially when using a high-resolution aerosol dataset to represent the aerosol direct effect and when using the Deng shallow cumulus scheme to represent the radiative effects of unresolved clouds. The improved aerosol treatment made a small but consistent and noticeable reduction in GHI errors in clear-sky conditions. The shallow cumulus scheme led to substantially reduced GHI errors when cloud cover was extensive, with errors roughly half as large as WRF-Solar without the shallow cumulus scheme.

Each of the four case days that we examined revealed various strengths and weaknesses of the component Sun4Cast nowcasting systems. At various times of day, lead times, and sky-cover regimes, different components do better or worse. This finding reinforces the need to

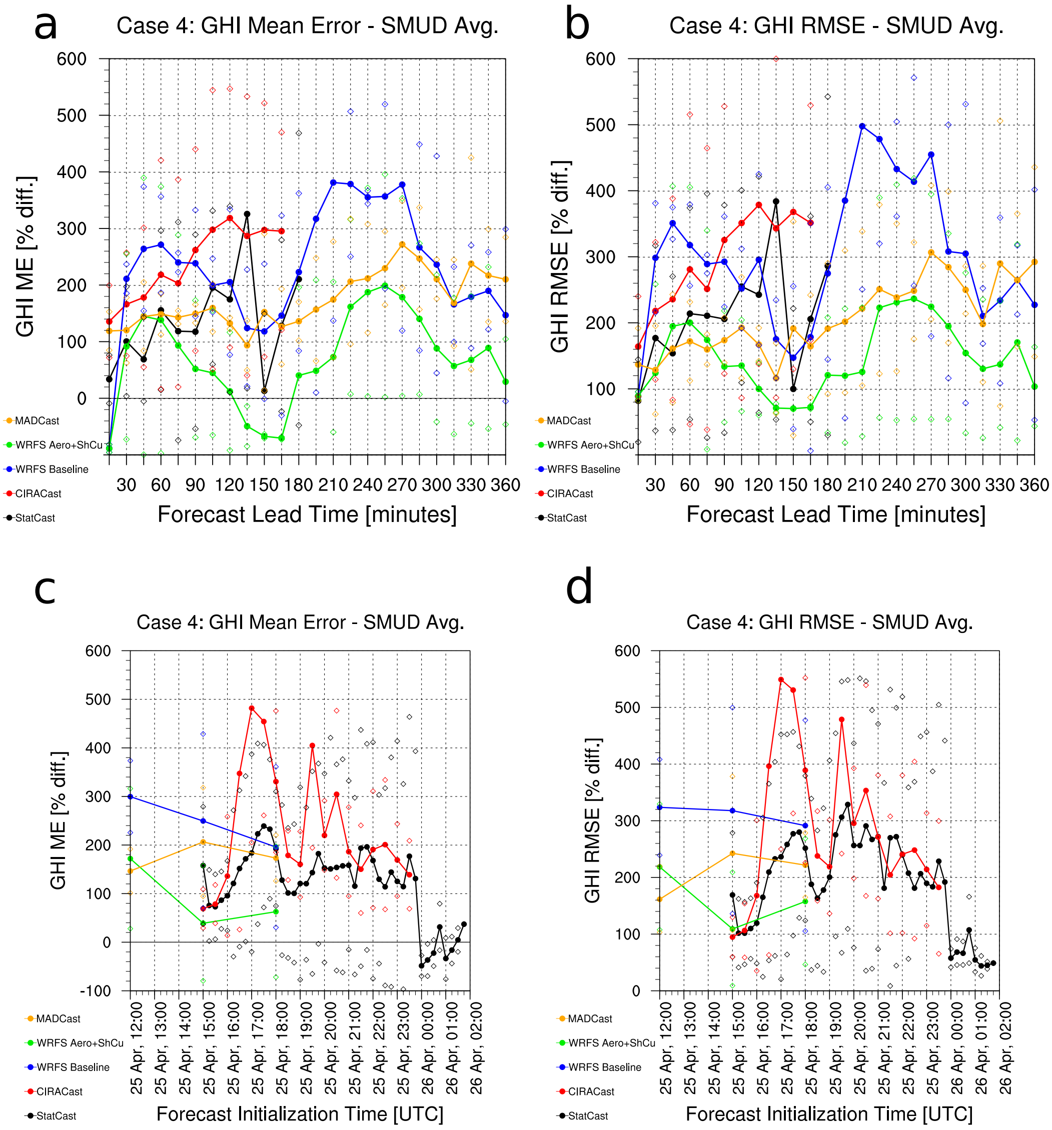

FIG. 21. As in Fig. 6, but for case 4.

include all these diverse components in the Sun4Cast system and also indicates the need to research and develop a dynamic weighting algorithm to make the most advantage of the strengths of each system.

This study did not conduct a comprehensive survey of all possible types of sky-cover situations. One would expect that NWP models would likely struggle with GHI predictions on days with new wildfires nearby because of the suddenly increased aerosol loading, whereas satellite-based models like CIRACast and MADCast that could identify and advect the smoke plume would do better on such days. Statistical learning methods like StatCast-Cubist, which incorporate the most recent hour of GHI observations, would also likely make a reasonable GHI forecast, even if similarly smoky conditions were not in the training dataset. This is a relevant consideration, especially in the arid western United States where wildfires are common every summer. Additionally, on days with a frontal passage and a distinct synoptic-scale cloud band or cloud field, satellite-based methods and NWP could be expected to perform well because of the inclusion of upstream cloud data, perhaps with some timing errors, while statistical learning methods may struggle. This further argues for the need for a diversity of techniques for forecasting GHI and the resulting power generated by solar plants, whether on a utility or distributed scale. A more exhaustive analysis of the performance of the various forecast components over a period of several months is available in Haupt et al. (2016).

Furthermore, in addition to the obvious impact for the solar energy community, improved irradiance forecasts, especially in NWP models like WRF-Solar, have benefits for a far wider set of forecast applications. Improving the irradiance forecasts will improve the surface energy balance modeling, which will in turn have impacts on applications ranging from soil and hydrologic modeling, to atmospheric boundary layer process modeling, to convective initiation modeling. Thus, continued research and development to improve irradiance forecasts will benefit the entire Earth and atmospheric sciences community.

Acknowledgments. This work was primarily funded by the U.S. Department of Energy's SunShot Initiative under Award DE-EE0006016, with additional funding provided by the National Science Foundation. We thank T. J. Vargas of the Sacramento Municipal Utility District for providing the GHI observations, Chris Gueymard of Solar Consulting Services for providing the aerosol datasets that form the basis of the monthly aerosol climatology in WRF-Solar, and Gael Descombes of NCAR for some assistance with MADCast. Computing resources for the MADCast and WRF-Solar runs were provided on Yellowstone (http://n2t.net/ark:/85065/d7wd3xhc), which is operated by NCAR's Computational and Information Services Laboratory and sponsored by the National Science Foundation. Additionally, all of the analysis and plotting scripts were coded using the NCAR Command Language (NCL; http://www.ncl.ucar.edu/). We also thank Branko Kosović of NCAR for a helpful internal review of the manuscript, in addition to two anonymous reviewers.

REFERENCES

Alapaty, K., J. A. Herwehe, T. L. Otte, C. G. Nolte, O. R. Bullock, M. S. Mallard, J. S. Kain, and J. Dudhia, 2012: Introducing subgrid-scale cloud feedbacks to radiation for regional meteorological and climate modeling. *Geophys. Res. Lett.*, **39**, L24809, doi:10.1029/2012GL054031.

Alessandrini, S., L. Delle Monache, S. Sperati, and G. Cervone, 2015: An analog ensemble for short-term probabilistic solar power forecast. *Appl. Energy*, **157**, 95–110, doi:10.1016/j.apenergy.2015.08.011.

Arbizu-Barrena, C., D. Pozo-Vázquez, J. A. Ruiz-Arias, and J. Tovar-Pescador, 2015: Macroscopic cloud properties in the WRF NWP model: An assessment using sky camera and ceilometer data. *J. Geophys. Res. Atmos.*, **120**, 10 297–10 312, doi:10.1002/2015JD023502.

Auligné, T., 2014a: Multivariate minimum residual method for cloud retrieval. Part I: Theoretical aspects and simulated observation experiments. *Mon. Wea. Rev.*, **142**, 4383–4398, doi:10.1175/MWR-D-13-00172.1.

——, 2014b: Multivariate minimum residual method for cloud retrieval. Part II: Real observations experiments. *Mon. Wea. Rev.*, **142**, 4399–4415, doi:10.1175/MWR-D-13-00173.1.

Benjamin, S. G., and Coauthors, 2016: A North American hourly assimilation and model forecast cycle: The Rapid Refresh. *Mon. Wea. Rev.*, **144**, 1669–1694, doi:10.1175/MWR-D-15-0242.1.

Buchard, V., and Coauthors, 2016: Evaluation of the surface $PM_{2.5}$ in version 1 of the NASA MERRA Aerosol Reanalysis over the United States. *Atmos. Environ.*, **125**, 100–111, doi:10.1016/j.atmosenv.2015.11.004.

Chow, C. W., B. Urquhart, M. Lave, A. Dominguez, J. Kleissl, J. Shields, and B. Washom, 2011: Intra-hour forecasting with a total sky imager at the UC San Diego solar energy testbed. *Sol. Energy*, **85**, 2881–2893, doi:10.1016/j.solener.2011.08.025.

Cintineo, R., J. A. Otkin, M. Xue, and F. Kong, 2014: Evaluating the performance of planetary boundary layer and cloud microphysical parameterization schemes in convection-permitting ensemble forecasts using synthetic *GOES-13* satellite observations. *Mon. Wea. Rev.*, **142**, 163–182, doi:10.1175/MWR-D-13-00143.1.

Delle Monache, L., T. Nipen, Y. Liu, G. Roux, and R. Stull, 2011: Kalman filter and analog schemes to postprocess numerical weather predictions. *Mon. Wea. Rev.*, **139**, 3554–3570, doi:10.1175/2011MWR3653.1.

——, F. A. Eckel, D. L. Rife, B. Nagarajan, and K. Searight, 2013: Probabilistic weather prediction with an analog ensemble. *Mon. Wea. Rev.*, **141**, 3498–3516, doi:10.1175/MWR-D-12-00281.1.

Deng, A., B. Gaudet, J. Dudhia, and K. Alapaty, 2014: Implementation and evaluation of a new shallow convection scheme in WRF. *26th Conf. on Weather Analysis and Forecasting/22nd Conf. on Numerical Weather Prediction*, Atlanta, GA, Amer. Meteor. Soc., 12.5. [Available online at https://ams.confex.com/ams/94Annual/webprogram/Manuscript/Paper236925/12%205_22nd_NWP_Conf_Deng_ExtendedAbstract.pdf.]

Descombes, G., T. Auligné, H.-C. Lin, D. Xu, C. Schwartz, and F. Vandenberghe, 2014: Multi-sensor Advection Diffusion Nowcast (MADCast) for cloud analysis and short-term prediction. NCAR Tech. Note NCAR/TN-509+STR, 21 pp., doi:10.5065/D62V2D37.

Diagne, M., M. David, P. Lauret, J. Boland, and N. Schmutz, 2013: Review of solar irradiance forecasting methods and a proposition for small-scale insular grids. *Renewable Sustainable Energy Rev.*, **27**, 65–76, doi:10.1016/j.rser.2013.06.042.

Haupt, S. E., 2013: A public-private-academic partnership to advance solar forecasting. *Proc. 42nd American Solar Energy Society Annual Conf.*, Baltimore, MD, American Solar Energy Society. [Available online at http://proceedings.ases.org/wp-content/uploads/2014/02/SOLAR2013_0284_final-paper.pdf.]

——, and B. Kosović, 2015: Big data and machine learning for applied weather forecasts: Forecasting solar power for utility operations. *Proc. IEEE Symp. Series on Computational Intelligence*, Cape Town, South Africa, IEEE, doi:10.1109/SSCI.2015.79.

——, and ——, 2016: Variable generation power forecasting as a big data problem. *IEEE Trans. Sustainable Energy*, doi:10.1109/TSTE.2016.2604679, in press.

——, and Coauthors, 2016: The SunCast solar power forecasting system: The results of the Public-Private-Academic Partnership to Advance Solar Power Forecasting. NCAR Tech. Note NCAR/TN-526+STR, 307 pp., doi:10.5065/D6N58JR2.

Heidinger, A. K., M. J. Foster, A. Walther, and X. Zhao, 2014: The Pathfinder Atmospheres–Extended AVHRR Climate Data Set. *Bull. Amer. Meteor. Soc.*, **95**, 909–922, doi:10.1175/BAMS-D-12-00246.1.

Huang, H., J. Xu, Z. Peng, S. Yoo, D. Yu, D. Huang, and H. Qin, 2013: Cloud motion estimation for short term solar irradiation prediction. Preprints, *IEEE Int. Conf. on Smart Grid*

Communications, Vancouver, BC, Canada, IEEE, doi:10.1109/SmartGridComm.2013.6688040.

Inman, R. H., H. T. C. Pedro, and C. F. M. Coimbra, 2013: Solar forecasting methods for renewable energy generation. *Prog. Energy Combust. Sci.*, **39**, 535–576, doi:10.1016/j.pecs.2013.06.002.

Jiménez, P. A., and Coauthors, 2016a: WRF-Solar: Description and clear-sky assessment of an augmented NWP model for solar power prediction. *Bull. Amer. Meteor. Soc.*, **97**, 1249–1264, doi:10.1175/BAMS-D-14-00279.1.

——, S. Alessandrini, S. E. Haupt, A. Deng, B. Kosović, J. A. Lee, and L. Delle Monache, 2016b: The role of unresolved clouds on short-range global horizontal irradiance predictability. *Mon. Wea. Rev.*, **144**, 3099–3107, doi:10.1175/MWR-D-16-0104.1.

Kleist, D. T., D. F. Parrish, J. C. Derber, R. Treadon, W.-S. Wu, and S. Lord, 2009: Introduction of the GSI into the NCEP Global Data Assimilation System. *Wea. Forecasting*, **24**, 1691–1705, doi:10.1175/2009WAF2222201.1.

Kuhn, M., S. Weston, C. Keefer, and N. Coulter, 2012: Cubist models for regression. R Project Doc., 18 pp. [Available online at https://cran.r-project.org/web/packages/Cubist/vignettes/cubist.pdf.]

Lara-Fanego, V., J. A. Ruiz-Arias, D. Pozo-Vázquez, F. J. Santos-Alamillos, and J. Tovar-Pescador, 2012: Evaluation of the WRF model solar irradiance forecasts in Andalusia (southern Spain). *Sol. Energy*, **86**, 2200–2217, doi:10.1016/j.solener.2011.02.014.

Lewis, J., R. De Young, R. Ferrare, and D. A. Chu, 2010: Comparison of summer and winter California central valley aerosol distributions from lidar and MODIS measurements. *Atmos. Environ.*, **44**, 4510–4520, doi:10.1016/j.atmosenv.2010.07.006.

MacDonald, A. E., C. T. M. Clack, A. Alexander, A. Dunbar, J. Wilczak, and Y. Xue, 2016: Future cost-competitive electricity systems and their impact on US CO_2 emissions. *Nat. Climate Change*, **6**, 526–531, doi:10.1038/nclimate2921.

Mahoney, W. P., and Coauthors, 2012: A wind power forecasting system to optimize grid integration. *IEEE Trans. Sustainable Energy*, **3**, 670–682, doi:10.1109/TSTE.2012.2201758.

Marquis, M., J. Wilczak, M. Ahlstrom, J. Sharp, A. Stern, J. C. Smith, and S. Calvert, 2011: Forecasting the wind to reach significant penetration levels of wind energy. *Bull. Amer. Meteor. Soc.*, **92**, 1159–1171, doi:10.1175/2011BAMS3033.1.

Mathiesen, P., and J. Kleissl, 2011: Evaluation of numerical weather prediction for intra-day solar forecasting in the continental United States. *Sol. Energy*, **85**, 967–977, doi:10.1016/j.solener.2011.02.013.

McCandless, T. C., S. E. Haupt, and G. S. Young, 2015: A model tree approach to forecasting solar irradiance variability. *Sol. Energy*, **120**, 514–524, doi:10.1016/j.solener.2015.07.020.

——, ——, and ——, 2016a: A regime-dependent artificial neural network technique for short-range solar irradiance forecasting. *Renewable Energy*, **89**, 351–359, doi:10.1016/j.renene.2015.12.030.

——, G. S. Young, S. E. Haupt, and L. M. Hinkelman, 2016b: Regime-dependent short-range solar irradiance forecasting. *J. Appl. Meteor. Climatol.*, **55**, 1599–1613, doi:10.1175/JAMC-D-15-0354.1.

Miller, S. D., D. Chand, C. L. Combs, M. Sengupta, and A. K. Heidinger, 2011: Toward evaluating short-term predictions of solar irradiance at the surface: Persistence, satellite-based trajectory and numerical weather prediction models. *Proc. 40th ASES National Solar Conf. 2011 (Solar 2011)*, American Solar Energy Society, 285–292. [Available online at http://www.proceedings.com/13815.html.]

——, M. A. Rogers, A. K. Heidinger, I. Laszlo, and M. Sengupta, 2012: Cloud advection schemes for short-term satellite-based insolation forecasts. *Proc. World Renewable Energy Forum*, Denver, CO, American Solar Energy Society, 1963–1967. [Available online at https://ases.conference-services.net/resources/252/2859/pdf/SOLAR2012_0385_full%20paper.pdf.]

Peng, Z., D. Yu, D. Huang, J. Heiser, S. Yoo, and P. Kalb, 2015: 3D cloud detection and tracking system for solar forecast using multiple sky imagers. *Sol. Energy*, **118**, 496–519, doi:10.1016/j.solener.2015.05.037.

Perez, R., S. Kivalov, J. Schlemmer, K. Hemker Jr., D. Renné, and T. E. Hoff, 2010: Validation of short and medium term operational solar radiation forecasts in the US. *Sol. Energy*, **84**, 2161–2172, doi:10.1016/j.solener.2010.08.014.

——, and Coauthors, 2013: Comparison of numerical weather prediction solar irradiance forecasts in the US, Canada and Europe. *Sol. Energy*, **94**, 305–326, doi:10.1016/j.solener.2013.05.005.

Pinker, R. T., and I. Laszlo, 1992: Modeling surface solar irradiance for satellite solar irradiance applications on a global scale. *J. Appl. Meteor.*, **31**, 194–211, doi:10.1175/1520-0450(1992)031<0194:MSSIFS>2.0.CO;2.

Quinlan, J. R., 1987a: Generating production rules from decision trees. *Proc. 10th Int. Joint Conf. of Artificial Intelligence*, Milan, Italy, 304–307. [Available online at http://ijcai.org/Proceedings/87-1/Papers/063.pdf.]

——, 1987b: Simplifying decision trees. *Int. J. Man-Mach. Stud.*, **27**, 221–234, doi:10.1016/S0020-7373(87)80053-6.

——, 1992: Learning with continuous classes. *Proceedings AI '92*, A. Adams and L. Sterling, Eds., World Scientific, 343–348. [Available online at http://sci2s.ugr.es/keel/pdf/algorithm/congreso/1992-Quinlan-AI.pdf.]

——, 1996: Improved use of continuous attributes in C4.5. *J. Artif. Intell. Res.*, **4**, 77–90.

Rienecker, M. M., and Coauthors, 2011: MERRA: NASA's Modern-Era Retrospective Reanalysis for Research and Applications. *J. Climate*, **24**, 3624–3648, doi:10.1175/JCLI-D-11-00015.1.

Rogers, M. A., S. D. Miller, J. M. Haynes, A. Heidinger, S. E. Haupt, and M. Sengupta, 2015: Improvements in satellite-derived short-term insolation forecasting: Statistical comparisons, challenges for advection-based forecasts, and new techniques. *Sixth Conf. on Weather, Climate, and the New Energy Economy*, Phoenix, AZ, Amer. Meteor. Soc., 6.4. [Available online at https://ams.confex.com/ams/95Annual/webprogram/Paper268850.html.]

Ruiz-Arias, J. A., J. Dudhia, and C. A. Gueymard, 2014: A simple parameterization of the short-wave aerosol optical properties for surface direct and diffuse irradiances assessment in a numerical weather model. *Geosci. Model Dev.*, **7**, 1159–1174, doi:10.5194/gmd-7-1159-2014.

Skamarock, W. C., and Coauthors, 2008: A description of the Advanced Research WRF version 3. NCAR Tech. Note NCAR/TN-475+STR, 113 pp., doi:10.5065/D68S4MVH.

Tegen, I., P. Hollrig, M. Chin, I. Fung, D. Jacob, and J. Penner, 1997: Contribution of different aerosol species to the global aerosol extinction thickness: Estimates from model results. *J. Geophys. Res.*, **102**, 23 895–23 915, doi:10.1029/97JD01864.

Tuohy, A., and Coauthors, 2015: Solar forecasting: Methods, challenges, and performance. *IEEE Power Energy Mag.*, **13**, 50–59, doi:10.1109/MPE.2015.2461351.

Urquhart, B., B. Kurtz, E. Dahlin, M. Ghonima, J. E. Shields, and J. Kleissl, 2015: Development of a sky imaging system for short-term solar power forecasting. *Atmos. Meas. Tech.*, **8**, 875–890, doi:10.5194/amt-8-875-2015.